Composites Part B

Carrot-based covalently bonded saccharides as a new 2D material for healing defective calcium-silicate-hydrate in cement: Integrating atomistic computational simulation with experimental studies

--Manuscript Draft--

Manuscript Number:	JCOMB_2020_303R2
Article Type:	Full Length Article
Keywords:	Calcium silicate hydrate; carrot nanomaterial; mechanical properties; molecular dynamics simulation; cementitious nanocomposites
Corresponding Author:	yin chi Wuhan University Wuhan, China
First Author:	yin chi
Order of Authors:	yin chi
	Bo Huang
	Mohamed Saafi
	Jianqiao Ye
	Colin Lambert
Manuscript Region of Origin:	Europe
Abstract:	Concrete is currently produced at a rate of 20 billion tonnes per year and contributes 5-10% of mankind's CO2 production. If the strength of the calcium-silicate-hydrate (C-S-H), the main binding material of concrete, could be improved, the volume of cementitious material needed for a given structure would be reduced and its environmental impact would be decreased. Here, we show that the constitutive behavior of C-S-H can be improved significantly by complexation with carrot-based cellulose nanosheets (CNSs). This environmentally friendly, reinforcing material heals the defective microstructure of C-S-H, which is responsible for structural deformation and failure at larger length scales. CNSs are built from repeating saccharide units that are covalently linked by a β-1-4 glycosidic (C-O-C) bond. The CNSs show remarkable affinity to C-S-H due to the interfacial Ca-O coordination and H-bond interaction. The functional groups on the surface of the CNS sheet act as a root network, cross-linking the neighboring silicate calcium layers and inhibiting the water dynamics at the silicate nanochannel, thereby significantly improving the interfacial properties of the C-S-H/CNS hybrid structure. The macro experimental results show that the mechanical properties of the composites increase with increasing the concentration of CNSs up to 0.4-wt%. At 28 days and CNS concentration of 0.20-wt%, the flexural strength increases by about 23.2% and the compressive strength increases by about 17.5%. The C-S-H/CNS composites show significant enhancement in strength, stiffness and ductility, and provide a foundation for the development of new high-performance construction materials with lower carbon footprint.
Suggested Reviewers:	Dongshuai Hou dshou@outlook.com Prof.Hou has professional expertise in MD simulation
	Patrick Dangla Patrick.Dangla@ifsttar.fr Prof.Patrick's expertise lie in the multiscale modelling of composite material
	Caijun Shi cshi@hnu.edu.cn Prof.Caijun Shi is an international renowned expert in cementitious composite material
	Mingzhong Zhang mingzhong.zhang@ucl.ac.uk Prof.Zhang has many experiences in modelling and characterization of fiber reinforced

Powered by Editorial Manager® and ProduXion Manager® from Aries Systems Corporation

	cementitious composite
	Xiangming Zhou xiangming.zhou@brunel.ac.uk Prof. Zhou's research covers a board range of fields in Construction Materials and technology, with focus on cement and concrete, and structural engineering application.
Opposed Reviewers:	
Response to Reviewers:	

Department of Engineering,
Lancaster University,
Lancaster,
LA1 4YB,
United Kingdom

Tel. +44 (0)1524 594070
Email: m.saafi@lancaster.ac.uk

14th January 2020

To: Editor-in-Chief
Dear Prof. Hao Wang,

It is a pleasure to submit our manuscript "Carrot-based covalently bonded saccharides as a new 2D material for healing defective calcium-silicate-hydrate in cement: Integrating atomistic computational simulation with experimental studies" for publication in Composite Part B: Engineering Journal.

There is an urgent need to reduce the carbon footprint of concrete production, which currently accounts for 5-10% of mankind's CO_2 production. Our combined experimental and theoretical study takes a significant step towards this goal by demonstrating that the flexural and compressive strengths of the calcium-silicate-hydrate (C-S-H) binding material of concrete can be improved significantly by complexing C-S-H with carrot-based cellulose nano sheets (CNSs). The latter are readily synthesised from waste food streams and are therefore environmentally friendly, abundant and inexpensive.

This unprecedented improvement in the strength of ordinary Portland cement means that the volume of concrete used in a given structure, and the associated CO_2 production, can be significantly reduced. Our molecular dynamics simulations reveal that the atomistic origin of this improvement is due to the interaction of CNSs with defects in C-S-H, which are the main cause of failure in the bare C-S-H.

We believe that this demonstration of a CNS reinforcement effect will be of interest to a broad readership of Composite Part B: Engineering, including materials modellers and experimentalists working on the rational design of cementitious materials with improved performance. Beyond academia, we expect that this will stimulate biomass processors and manufacturers of cementitious materials to collaborate in the development of this new composite material.

Best regards,

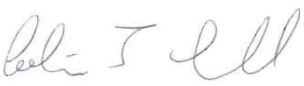

Professor M. Saafi and Dr.Yin Chi

Responses to reviewers' comments on manuscript 1st revision

Journal: Composites Part B: Engineering
Manuscript number: JCOMB_2020_303
Title: Carrot-based covalently bonded saccharides as a new 2D material for healing defective calcium-silicate-hydrate in cement: Integrating atomistic computational simulation with experimental studies
Authors: *Yin Chi, Bo Huang, Mohamed Saafi, Jianqiao Ye, Colin Lambert*

The authors would like to thank the editor and reviewers for their careful reading of our manuscript and thoughtful comments, and valuable suggestions to further improve the quality of our paper. We addressed all comments in the revised manuscript. The table below lists our response to the reviewers' comments. The basic format follows the sequence: Comments, Response and Corrections. The revised text is marked in blue.

Responses to reviewer's comments

No.	Comments, Reply and Corrections	
1.	Comments	*In this paper, by combining experiments and molecular dynamics simulation, the authors investigate the complexation of carrot-based cellulose nanosheets (CNS) and calcium-silicate-hydrate (C-S-H). Authors found that this reinforcing material can heal the defective microstructure of C-S-H, which is responsible for structural deformation and failure at larger length scales. And the molecular modelling was used to reveal the microstructures. This paper has appropriate methods and interested topic. And the manuscript is well revised. I suggest that this paper is published after minor revised. There are some point that authors may want to further improve:* *1. There is not well correspondence between RDF and microstructure. For example, the RDF between Oc and Hw seems to be more dominant, but the first peak is given in the microstructure snapshot. How did authors explain that?*
	Response	Thank you very much for your recognition of our work. (1) We apologize for the confusions made to the reviewer. Actually we cannot quantitatively judge the dominance of the atomic connection density through microstructural observations. Whilst RDF pattern can realistically evaluate the connection that describes how atom density varies as a function of distance from a referenced atom. Microstructure observation can only act as a complementary reference to understand the atomic bond connections. (2)The microstructure snapshots in the Fig.7 are screened from a perspective view, where we would like to show the typical connections of the H bond types from different oxygen and hydrogen species within the CNS/C-S-H composite system, when one kind of connection is shown, the other types are set as invisible. (3) From Fig.7, It is reasonable that the RDF of Oc and Hw is more dominant

		with peak position less than the others, which is also in consistence with the partial charge differences of the atoms based on the force field parameters. This is because Oc has higher positive partial charge in comparison to the Ow species.
	Corrections	We modified Fig.7 and added another three microstructure snapshots that are in correspondence to the Oh-Hw, Ow-Hc, Ow-Ho connections respectively. The text in the manuscript is also corrected correspondingly. 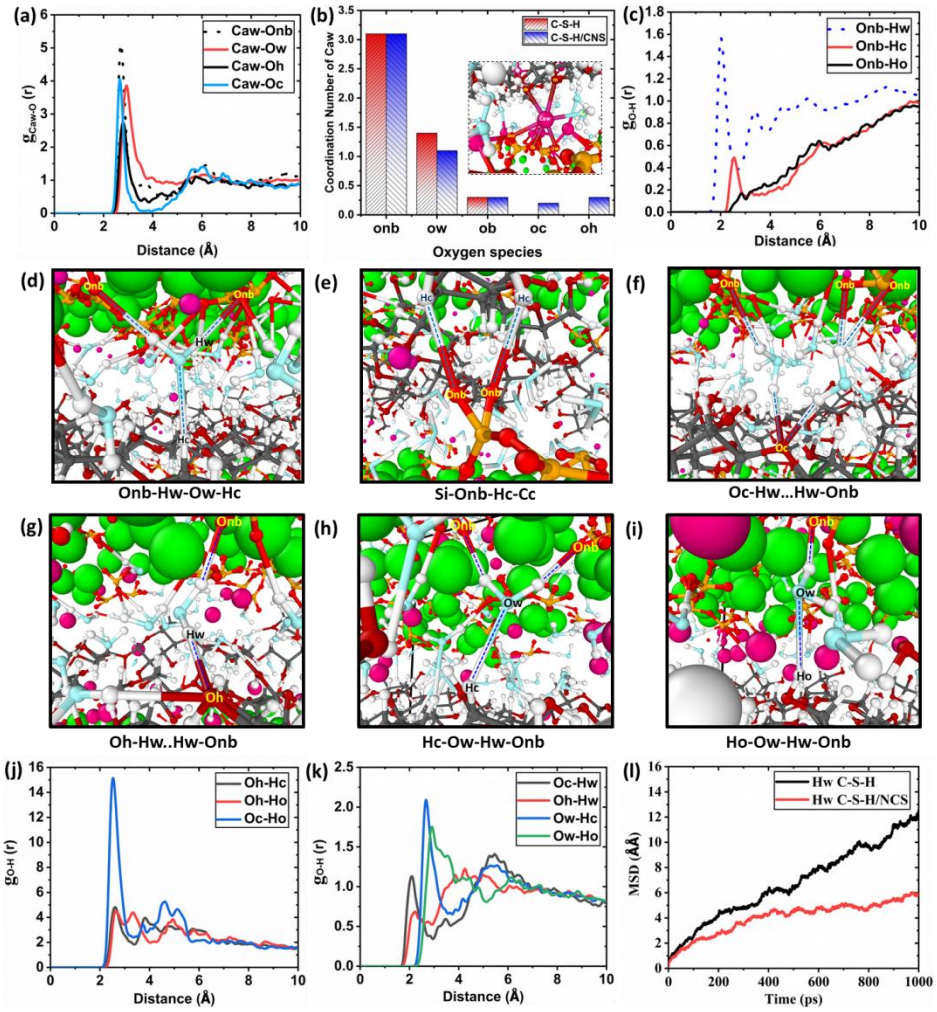 Fig.7
2.	Comments	*MSD is not stable, does it indicate that the system has not reached equilibrium?*
	Replies	Thank you for the comment. As a matter of fact, we cannot directly justify whether the system has reached the equilibrium through the MSD value. The equilibrium state of the nanocomposite can be determined through monitoring the evolution of the potential energy of the entire molecular system. For example, the Fig.r1 given below illustrates the typical potential energy evolution process of the CNS/C-S-H molecular system with C/S=1.7 over simulation time steps. It can clearly be seen that the potential energy of

		the system is first decreased rapidly followed by a steady decrease with a slow rate over time steps of 2000000(1 nanosecond simulation time). It is true that the potential energy of the molecular system can be further reduced upon more relaxation time, whilst the reduction can be very small. Therefore we assume in the current study that 1 nanosecond relaxation is enough for the system to reach a relative stable state. 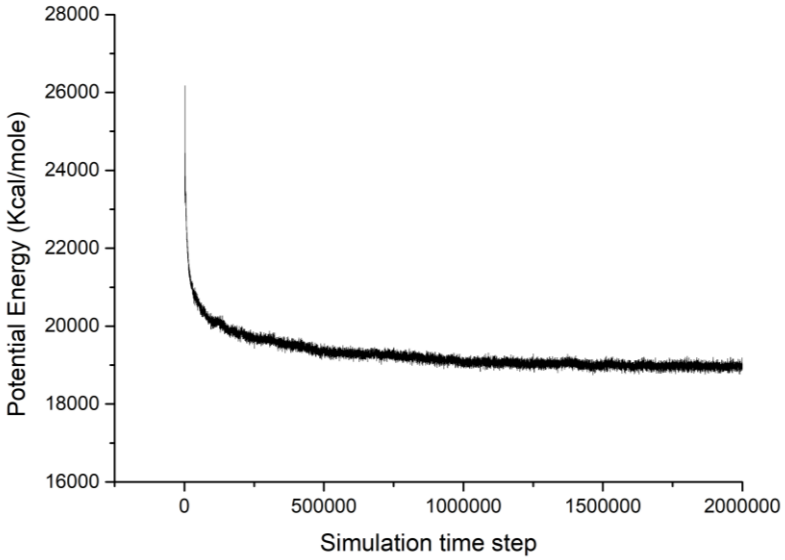 Fig.r1 Potential energy evolution of the entire molecular system of CNS/C-S-H nanocomposite having C/S ratio of 1.7
	Corrections	No changes have been made in the text.

Graphical Abstract

Graphic abstract

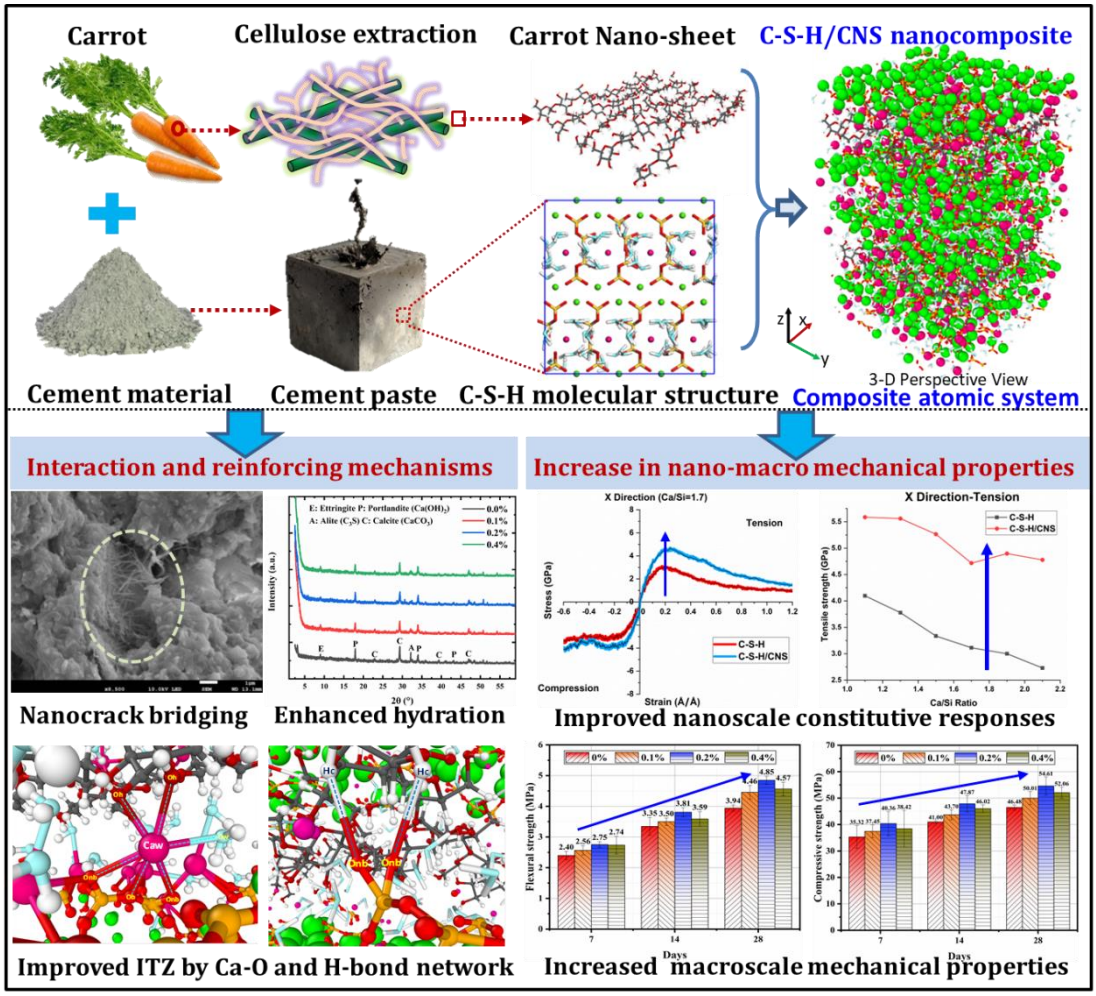

Manuscript File
Click here to view linked References

Carrot-based covalently bonded saccharides as a new 2D material for healing defective calcium-silicate-hydrate in cement: Integrating atomistic computational simulation with experimental studies

Yin Chi,[a,b*] *Bo Huang,*[b] *Mohamed Saafi,*[b]* *Jianqiao Ye,*[b] *Colin Lambert* [c]

[a] School of Civil Engineering, Wuhan University, Wuhan 430072, China
[b] Department of Engineering, Lancaster University, Lancashire, LA1 4YW, UK
[c] Department of Physics, Lancaster University, Lancashire, LA1 4YB, UK

ABSTRACT:

Concrete is currently produced at a rate of 20 billion tonnes per year and contributes 5-10% of mankind's CO_2 production. If the strength of the calcium-silicate-hydrate (C-S-H), the main binding material of concrete, could be improved, the volume of cementitious material needed for a given structure would be reduced and its environmental impact would be decreased. Here, we show that the constitutive behavior of C-S-H can be improved significantly by complexation with carrot-based cellulose nanosheets (CNSs). This environmentally friendly, reinforcing material heals the defective microstructure of C-S-H, which is responsible for structural deformation and failure at larger length scales. CNSs are built from repeating saccharide units that are covalently linked by a β-1-4 glycosidic (C-O-C) bond. The CNSs show remarkable affinity to C-S-H due to the interfacial Ca-O coordination and H-bond interaction. The functional groups on the surface of the CNS sheet act as a root network, cross-linking the neighboring silicate calcium layers and inhibiting the water dynamics at the silicate nanochannel, thereby significantly improving the interfacial properties of the C-S-H/CNS hybrid structure. The macro experimental results show that the mechanical properties of the composites increase with increasing the concentration of CNSs up to 0.4-wt%. At 28 days and CNS concentration of 0.20-wt%, the flexural strength increases by about 23.2% and the compressive strength increases by about 17.5%. The developed atomic-scale molecular dynamics simulations, combined with top-down experimental measurements of their mechanical properties reveal that the proposed C-S-H/CNS composites

show significant enhancement in strength, stiffness and ductility, and provide a foundation for the development of new high-performance construction materials with lower carbon footprint.

Keywords: calcium silicate hydrate, carrot nanomaterial, molecular dynamics simulation, mechanical properties, cementitious nanocomposites

Correspondence: Prof. M. saafi, E-mail: m.saafi@lancaster.ac.uk, Tel: +44 (0)1524 594070. Dr. Yin Chi, Email: yin.chi@whu.edu.cn, Tel: +86(27)68775337,

1. Introduction

The growing global need for sustainable and environmentally friendly civil infrastructure is driving the development of high-performance construction materials that have high durability and low carbon footprint[1]. Significant past research has been directed at improving the performance of Ordinary Portland Cement (OPC), the most wid ely used manmade material on earth, by enhancing the nano-micro scale physico-mechanical properties of calcium silicate hydrate (C-S-H), which is the main binder that ‘glues’ the other key ingredients (i.e. sand and gravel) of concrete. For example, nano additives derived from silica aluminate, titanium dioxide and calcium carbonate to mention a few[2–5] were used to accelerate the hydration of OPC and increase the amount of C-S-H which in return improves the bulk properties of the cementitious composites. Novel 1D materials such as carbon nanotubes (CNTs) and 2D materials such as graphene, graphene oxide (GO) and hexagonal boron nitride (h-BN) have been extensively used to create intercalated nanostructures in cement matrix composites (CMCs)[6–13]. The resulting nanoengineered CMCs exhibited improved mechanical performance and durability. Other additives in the form of organic polymers such as poly vinyl alcohol(PVA), poly ethylene glycol (PEG) and poly acrylic acid (PAA) as well as polycaboxylate materials[14–19] were utilized as nano inclusions to improve the fracture energy and toughness of OPC by modifying the microstructure of C-S-H.

Analytical characterization tools coupled with advanced modeling and experimental techniques[20–25] from molecular-scale to macro-scale were used to elucidate the chemical and physio-mechanical properties of these engineered cementitious composites and provide a bottom-up multi-scale composite optimization and damage analysis approach[26–31].

However, the broad industrial application of these nano-modified cementitious composites currently face several hurdles: first, the nanomaterials exhibit poor dispersion capacity in the CMCs as well as tend to agglomerate at high concentrations, leading to the formation of unexpected micro defects and nonhomogeneous microstructure development in the composite systems[32]. The use of CNTs, graphene, GO and h-BN as well as the organic polymers are found to lack strong interfacial adhesion with C-S-H, thereby providing limited performance enhancement of cementitious materials. More importantly, current nanomaterials are expensive to produce and require intensive energy during manufacturing processes. They also pose significant environmental, health and safety risks.

Another way to improve the performance of OPC composites is to reduce defects in C-S-H resulting from a very high calcium-silicate ratio (Ca/Si)[23,33]. Qomi et al.[34] and Pellenq et al.[35] used molecular dynamics (MD) simulations to show that reducing the Ca/Si ratio of C-S-H from 2.1 to 1 would significantly increase its stiffness and strength. However, reducing the Ca/Si ratio by tailoring the microstructure and altering the cement chemistry at an atomic scale is challenging and is impractical for large scale applications.

Cellulose-enhanced CMCs have received a great deal of attention as an attractive alternative to CMCs reinforced with CNTs, graphene, GO or h-BN[36–41]. This is because cellulose-based nanomaterials are abundant, environmentally friendly, inexpensive, highly dispersible in concrete and exhibit better affinity to C-S-H due to their oxygen functional groups. Recently, we demonstrated that when added to CMCs, 2D nano-platelets synthesized from sugar-beet root pulp become bound to C-S-H through hydrogen or ionic/covalent bonds thus forming a three-dimensional network[42]. However, the high concentration of hydroxymethyl functional groups in the sugar-beet fructose unit resulted in significant agglomeration of the sheets in the CMC, which led to inefficient healing of the defective C-S-H as witnessed by the reduction in the mechanical properties of the 2D-sugar beetroot sheet-reinforced cementitious composites[42]. The majority of literature focuses on the use of

different experimental and simulation methods to determine the nanoscale properties of 1-D cellulose crystals[43–45] and C-S-H[46–49]. However, to the authors' knowledge, the properties of bio-based 2D-nanomaterials and their interactions with C-S-H have not been investigated, thus delaying their application in cementitious composites.

In this paper, we present a newly developed CMC reinforced with highly water dispersible 2D carrot-based nanosheets (CNSs) synthesized from carrot waste streams. We perform molecular dynamics simulations combined with experimental characterization to elucidate how the CNSs interact with the defective microstructure of C-S-H. Our atomistic modeling provides fundamental understanding of how the C-S-H/CNS complexes are formed at a molecular-level and how they are translated into interfacial bonding and strength in nanostructured hybrid CMCs with different Ca/Si ratios.

2. Materials and method

2.1 Preparation of carrot-based cellulose nanosheets

The CNSs were fabricated from waste biomass by our industrial partner Cellulocomp L.L.C. (UK) following the procedure developed for sugar beetroot sheets as detailed in[42,50]. The fabrication process is shown in Fig.1. In this process, carrot samples were first treated with sodium hydroxide (0.5mol) where the hemicellulose and pectin were extracted from the plant cells. Subsequently, the solution was heated to 90^{o}C for a period of 5 hours and followed by 1 hour homogenization using a rotating mixer with the rate set varying between 11 and 30 m/s. This achieves the separation of the cells along the line of the middle lamella and results in formation of cell sheets. The carrot sheets were separated from the dissolved materials using a filtration process[50]. The final product is a stable CNS suspension solution with 4% CNS solid and 96% water. A commercial nonionic surfactant was also added to the solution to reduce cellulose aggregation thereby allowing CNSs to be readily dispersed in the aqueous

solutions for a long period of time. This as-received CNS suspension was then used as the additive to prepare the cementitious nanocomposites.

2.2 Preparation of cement pastes

The cement pastes were prepared using ordinary Portland cement (OPC) type CEM I 52.5N. A water-to-cement ratio of 0.35 was used and kept constant for all mixes. The as-received CNSs suspension was first added into the required water with superplasticizer, and the resulting aqueous solution was mildly sonicated for 30 min. The obtained suspensions were then blended with cement powder and mixed for 10 min to prepare the cementitious composite mixtures. The pastes were then poured into plastic molds to fabricate the specimens, which were then shaken for 1 min using a vibrating machine. After 24 hours of curing, the specimens were demolded and cured in the laboratory. For each concentration, prisms (40 mm× 40 mm× 160 mm) and cubes (50 mm × 50 mm × 50 mm) were cast and cured in warm water of a temperature of 20^{o}C to testing for mechanical properties.

2.3 Experimental characterization of cement pastes

The effect of the CNS inclusion on the performance of the cementitious composites was examined. A total of 36 (50×50×50 mm) cube samples were tested at 7, 14, and 28 days to determine their compressive strength. The compression tests were performed using an universal servo-controlled testing system (UTM, Instron 8802J5219, 250KN) according to ASTM C-109[51] with a loading rate of 0.5MPa/s. Thirty-six (40×40×160 mm) prisms were also tested under a four-point bending test at 7, 14 and 28 days to determine their flexural strength. The four-point bending tests were carried out using an ASTM Zwick Roell Z020 machine (C090204019, 20KN, Germany) according to ASTM C78[52]. The tests were conducted using a displacement control with a rate of 0.1 mm/min.

Scanning electron microscopy (SEM) fitted with X-ray Energy Dispersive Spectrometer (EDS) (JSM-7800F) in combination with X-ray diffraction (XRD) (Agilent SuperNova) was used to identify the chemical composition and the microstructure of the hardened cement pastes. Fragments of the samples obtained from the mechanical testing were dried in a vacuum oven for 24 hours at 80° C and coated with gold before imaging. The working voltage ranged from 5kV to 15kV. XRD patterns were recorded at a scanning rate of 2°/min from 2θ=5° to 90° with Cu Kα radiation (λ = 1.5418 Å) on Single crystal.

2.4 Computational methodology

The MD simulations were performed using LAMMPS[53]. Graphic processing of the molecular features was achieved by the open visualization tool OVITO[54]. The stable configurations (i.e., bond, angle, dihedral etc.) with minimum energy were attained by relaxing the composite systems at the beginning of the calculations. In these simulations, the non-linear conjugate gradient (CG) algorithm with an energy tolerance of 10^{-6} Kcal/mole and a force tolerance of 10^{-6} Kcal/mole-Angstrom were used in combination with the isothermal-isobaric (NPT) ensemble for 200000 steps at T=300 Kelvin without external constraint. The time step was fixed at 0.5 femtosecond, and a built-in Noose-Hoover style themo/barostatting with a Verlet time-integration scheme was applied throughout the molecular dynamics simulations. Finally, another 1000 picoseconds run was conducted for the results acquisition. The molecular configurational information and atom dynamic properties were collected every 5 picoseconds for the statistical analysis. For uniaxial tensile and compressive tests, the strain rate was set as 0.008 Å per picosecond and the periodic boundary condition (PBC) was used to simulate the applied load conditions. During deformation in one direction, the pressures at the other two directions were maintained at zero, allowing the

system to relax without external constraint. The stress–strain curves were captured by recording the pressure development along the load direction as a function of the applied strain. The elastic modulus was calculated from the slope of the linear regime of the stress-strain curve.

3. Results and discussions

3.1 Measurements of micro-structural and mechanical properties

The hierarchical structure, molecular model and SEM micrographs showing the morphology of the CNS are depicted in Fig. 2. The CNS is formed from repeating saccharide units that are covalently linked by a β-1-4 glycosidic(C-O-C) bond (Fig. 2a). The water-based CNS suspension (Fig. 2b) was obtained by the chemical process detailed in the experimental section. The chains are stacked tightly during the biosynthesis process, resulting in the formation of semi-crystalline CNS sheets. As shown in Fig. 2b, the resulting CNS sheets are composed of randomly oriented nanofibrils and their glucose units with symmetrical structure at molecular scale contain less hydroxymethyl groups[55,56] in comparison to the sugar-beet fructose unit, enabling more uniformly dispersion throughout the CMCs. The molecular structure of the CNS and the corresponding chemical stoichiometry of one saccharide unit (Fig. 3) are used to perform MD simulations aimed at probing the behavior of the C-S-H/CNS complexes at atomic level. This provides valuable insight into the interaction and reinforcing mechanisms in the C-S-H/CNS composite, and the nanoscale stress-strain response under different uniaxial tension/compression loading scenarios and Ca/Si ratios.

Firstly, XRD was employed to characterize the change in the microstructure and the hydration phases of the CMCs as a result of the addition of CNS sheets. The XRD patterns of the C-S-H/CNS nanocomposites at CNS concentrations of 0.00, 0.10 and 0.20-wt% at 28 days of curing are shown in Fig. 4a. All samples exhibited similar phases, including ettringite, calcium hydroxide $Ca(OH)_2$, un-hydrated tricalcium silicate (C_3S) and calcium carbonate ($CaCO_3$). The C-S-H hydration phases cannot be identified because of their semi-crystalline

nature. However, their improved growth as a result of the addition of CNS can be quantified by examining the change in the detected crystalline phases of the cementitious composites. Based on the XRD results together with the assorted CrysAlisPro software analysis, we quantitatively identified the proportion of the hydration phases. It is found that the quantities of ettringite, $Ca(OH)_2$ and other crystals increase, while the un-hydrated phases C3S and $CaCO_3$ diminish due to the addition of CNS. It can be hypothesized that the addition of CNSs can accelerate the hydration process and result in an increase in the formation of these hydration phases and particularly the amplification of C-S-H growth. The authors are currently testing this hypothesis through in depth experiment characterizations(e.g., TGA/XRD techniques[57]) and reactive MD simulations, which will be discussed in a subsequent publication. Here, we conjecture that the high cement alkaline environment (with pH=11.7) rich in Ca^{2+} ions attenuates/dissolves the acid hydroxyl/hydroxymethyl functional groups on the surface of the CNS sheets. This mechanism can occur during the interaction between the cellulose and cement, where the Ca ions react with the dissolved hydroxyl groups to precipitate the formation of $Ca(OH)_2$[42]. The dissociation of functional groups from the CNS typically contributes to the concentration of hydroxyl groups in the solution, which may accelerate the hydration process of cement particles.

Fig. 4b shows SEM images of the nanocomposites along with their corresponding EDX spectra and oxygen maps at mass fractions of 0.00 and 0.40-wt% at 28 days. The microstructure of CMC with 0.00-wt% mainly contains un-hydrated cement particles, micro-cracks and $Ca(OH)_2$, whereas the microstructure of CMC with 0.40-wt% contains dense C-S-H gels with embedded CNSs to form intercalated nanocomposites. From the EDX spectrum, we can see that the addition of the CNSs increases the content of carbon in the cementitious composite. The oxygen map shows that the cementitious composite with CNSs has denser and more uniformly distributed oxygen peaks. This can be attributed to the excellent uniform distribution of the CNSs within the CMCs.

The effects of the CNSs on the flexural and compressive strengths of the cementitious composites at 7, 14 and 28 days are shown in Fig. 4c,d. As depicted, the flexural strengths increase with increasing the concentration of CNSs, reaching an increase of 14.6%, 13.7%, 23.2% respectively at 0.20-wt% due to both the reinforcing effect and the amplification of C-S-H growth resulting from the CNSs. Similar trend is also observed for the compressive strengths where a maximum improvement of about 17.5% at 0.20-wt% is obtained. It indicates that the morphology of the microstructure of the cementitious composites containing CNSs is more effective in resisting tensile stress than compressive stress due to the crack bridging effect of the CNSs. However, the mechanical properties are decreasing when the CNS concentration rises to 0.4-wt% for all the cases. We hypothesize that at a relative higher CNS concentrations (0.4-wt%), stacking of the CNS sheets may occur in the cementitious composite. As a matter of fact, the high cement alkaline environment that is rich in Ca^{2+} ions captures and attenuates the acid hydroxyl/hydroxymethyl functional groups on the surface of the CNS sheets. This increases the hydrophobicity of CNS due to the carbon rich backbone chain, as a consequence, high van der Waals repulsive forces are created thereby allowing the CNS sheets to stack and agglomerate. When high CNS concentrations are present, agglomerations of CNS tend to form and more defects can be formed within the cementitious composites thus deteriorating their mechanical properties as a result.

3.2 Atomistic simulations of C-S-H/CNS microstructure.

On the basis of the knowledge gained from the macroscale experimental results, we performed MD simulations to uncover the interactions and reinforcing mechanisms at atomic-scale in the bilayer C-S-H/CNS structure. Using the tobermorite 11 Å model proposed by Hamid as an atomic structural benchmark[58], we constructed C-S-H substrate and C-S-H/CNS nanocomposite models with six Ca/Si ratios ranging from 1.1-2.1, which cover the typical range known from experimental observations of different C-S-H products. The critical textural information of the constructed C-S-H molecular model, including the mean

chain length (MCL) and H_2O/Si ratio, is shown in Fig. S1 and Table S1 in the supporting information. The SEM images in Fig. 5a,b demonstrate the intercalation of the CNS chains in the basal structure of C-S-H. This can be further confirmed by examining the XRD patterns of the cementitious composites. Fig. 5c shows the zoomed-in XRD patterns from 2.5 to 6° 2θ and reveals that the XRD pattern of the plain cementitious composite shows a hump-like peak around 3° 2θ. When the CNSs are present, this peak becomes broader and less intense, indicating the existence of bilayer C-S-H/CNS crystals in the cementitious composites. Based on this behavior, we constructed a molecular model for the C-S-H/CNS nanocomposite as illustrated in Fig. 5d. The manipulation process of the nanocomposite molecular model is given in Fig. S2. The bonded and non-bonded interactions in the molecular system are defined by a combinational set of parameters from both the ClayFF force field[59], and the Consistent Valence Force Field(CVFF)[60]. We used the classic Simple Point Charge (SPC) model for representing the water, hydroxyl and oxygen-oxygen interactions[61]. The nanocomposite systems were then relaxed in order to attain stable and minimum energy configurations. Uniaxial tension and compression tests were subsequently performed along the *x*-, *y*- and *z*-directions.

Taking the C-S-H/CNS nanocomposite with a median Ca/Si ratio of 1.7 as an example, a typical minimized 3D configuration of the C-S-H/CNS nanocomposite after NPT equilibrium (constant atom number, pressure and temperature) is shown in Fig. 6. This shows that each CNS is in close contact with the neighboring calcium silicate sheet and is highly distorted and wrinkled, exhibiting a pronounced surface disturbance. The different functional groups of the CNSs, including the hydroxymethyl group(-CH_2OH), hydroxyl group(-OH) and methine group(-H), protrude towards the C-S-H surface and point towards the vacancies of the interlayer water nanometer channel. The initial cleaved nano-pore sized vacuum space in C-S-H is completely closed with the original flat CNSs distorting into an amorphous 3-D carbon-oxygen network structure (see Fig. 6a), implying that a strong binding has been

established between the CNS and the C-S-H. From Fig. 6b, there is a sharp peak in the carbon atom density distribution, with only a small overlap with the density profiles of the interlayer calcium (Caw) ions and water hydrogen (Hw) in the C-S-H model. However, the intensity of both the hydrogen atoms bonded to the CNS glucopyranose ring (Hc) and the hydrogen atoms from the hydroxyl/hydroxymethyl functional groups (Ho) show broader distributions than the backbone carbon atoms (Cc), and their profiles have more overlap with that of Caw. The density profile of Hc from the CNS methine group possesses higher peak and covers the same range as that of Ho from both hydroxymethyl/hydroxyl groups, exhibiting similar binding affinity with the calcium silicate sheets. From Fig. 6b, the presence of Hw atoms in the CNS chain backbone region, indicates that the water molecules migrate from the C-S-H gel and penetrate into the CNS molecular structure. This is attributed to the strong hydrophilic characteristics of the CNS. This is significant, because removing water from C-S-H would reduce its brittleness, enhance its ductility and strengthen the C-S-H/CNS interface owing to the increased Ca-O bonds as discussed below[62].

Fig. 6c illustrates the atom density distribution of the oxygen species from both the CNS and the C-S-H. It is noteworthy that apart from the oxygen atoms from the functional groups (Oh), the glycoside linkage oxygen and ring oxygen (backbone oxygen Oc) atoms are barely interacting with the calcium silicate surface. However, these groups actually weaken the electrostatic repulsion between the carbon atoms and the interlayer calcium cations at the silicate surface, thus contributing further to the connectivity of the CNS to C-S-H. Fig. 6c also shows that the Oh and the Ow atoms are located closer to the silicate non-bridging oxygen (Onb). Therefore, the water molecules, Caw cations, the functional groups of the CNS, the bridging silicate tetrahedra are the main atomic interactions at the interfacial transition zone (ITZ).

Fig. 7 depicts the atomic interactions at the C-S-H/CNS interface. The radial distribution function (RDF) patterns between the Caw and different oxygen species at the interlayer region

of C-S-H are depicted in Fig. 7a. The Caw cations in the C–S–H gel play a key role in crosslinking the neighboring calcium silicate sheets and also are responsible for the interfacial strength between the CNS and C-S-H. From Fig. 7a, one can see that the pronounced peaks in the RDF appear at a Ca-O distance around 2.7 Å for all the four Caw-O RDF patterns, indicating the existence of Ca-O ionic bonding network at the C-S-H/CNS interface. The bond length of Caw-Oh has almost the same value as Caw-Onb with relatively lower peak intensity. As expected, the Caw atoms energetically prefer the Oh atom of CNS. The interlayer Caw atoms are also strongly attracted by the backbone Oc and are orderly arranged in the vicinity of the CNS monolayer due to the electronegativity of the Oc atoms. The bond length order of Caw-O in the ITZ region ranks as follows: Onb>Oc>Oh>Ow. Therefore, the non-bonded ionic interaction between Caw and O species are critical in bridging the silicate tetrahedra and the CNS by forming a stable Si-O-Ca-O-C connection network.

The calculated average oxygen coordination number of Caw with a cutoff distance of 3 Å is shown in Fig. 7b. In the pure C-S-H model, the Caw atoms are coordinated to around 4.8 oxygen neighbors according to different surrounding chemical environments. The coordinated oxygen species are composed of 3.1 Onb, 1.4 Ow and 0.3 Ob (the bridging oxygen in pairing silicate tetrahedra). For the bilayer C-S-H/CNS nanocomposite, the Caw atoms are linked to a higher coordination number of 5 adjacent oxygen neighbors, containing two extra oxygen species, i.e., Oh and Oc from the CNS chain. The coordination number of the Caw in the equilibrated nanocomposite involves 3.1 Onb, 1.1 Ow, 0.3 Ob, 0.2 Oc and 0.3 Oh. The change in the coordinated oxygen species also confirms the established strong ionic connection between the C-S-H substrate and the CNS. The presence of the CNS at the silicate channel can increase the distance between Ow and Caw, which is regarded a key reason for the decreased Ow coordination number in the nanocomposite. In addition, the migration of water to the CNS surface due to the CNS hydrophilicity is also considered as an important reason for the Ow coordination reduction. From the inset picture in Fig. 7b, the Ca atoms clustered

with surrounding oxygen atoms having 6- to 7-fold coordination can form disordered octahedrons, leading to a more amorphous interfacial structure and strengthened C-S-H/CNS interface. This was also observed in previous studies[63].

In addition to the Ca-O ionic bond interaction, the hydrogen-bonding are also an important counterpart in crosslinking the C-S-H and the CNS. Fig. 7c shows the RDF patterns between different hydrogen species versus Onb atoms from C-S-H. The first peak in the RDF of Onb-Hw distributing from 1.7 to 2.4 Å, indicates the strong H-bond interaction between the silicate tetrahedral oxygen and surrounding water hydrogen atoms. The Hc atoms also have relative strong correlation with the Onb atoms. The defective silicate chains in the C-S-H offer a great number of non-bridging oxygen sites to accept H-bonds from the abundant methine functional groups of the CNS. The Hc atoms not only donate H-bonds and contribute to the affinity of the CNS to the C-S-H substrate surface, but also improve the interfacial property by forming a Si-O-H-C like connection system that is directly crosslinking the CNS and the C-S-H substrate surface. The representative local H-bond in the ITZ is illustrated in Fig. 7d-i.

In addition, it is noticed from Fig. 7c that the Ho atoms from the hydroxymethyl/hydroxyl functional groups of CNS have peculiar inconspicuous correlation with the non-bridging oxygen. This is attributed to the most of H-bond accepting sites from the silicate chains being occupied by the water molecules that restrict the mobility of the CNS functional groups. The obscure Onb-Ho bond is also due to the constraint of intra- molecular hydrogen bonds within a single CNS chain as well as the inter-molecular hydrogen bonds between the adjacent chains. These inter- and intra- molecular H-bonds within the CNS help maintain its integrity without de-protonation of the functional groups, whose patterns are schematically illustrated in Fig. S3. The RDF pattern shown in Fig. 7j further confirms the strong spatial correlation between Oc and Ho within the CNS. As can be seen, there is a sharp peak at a short range distance of 2.5 Å, primarily contributed by the O3-HO3…O5

intra-molecular hydrogen bond connection. This connection is highly stable during the deformation, which helps the nanocomposite resist the tensile stress along the chain direction.

Fig. 7k shows that there are strong short-range spatial correlations between oxygen from CNS and the hydrogen from water, as well as the oxygen from water and the hydrogen from the CNS molecular structure. The initial peaks of O_{CNS}-H_w are positioned at around 2 Å, and further positions of O_w-H_{CNS} are observed, implying that the CNS is more likely to act as H-bond acceptor. The oxygen in the CNS can provide an H-bond accepting site and is prone to connect water hydrogen Hw to form an O-Hw-Hw-O like linkage. The CNS can also donate H-bonds to the Ow mainly via methine groups of CNS, thereby crosslinking the neighboring silicate tetrahedral by H-Ow-Hw-O connections. As a consequence, the bulk water in the interlayer region of C-S-H serves as an aqueous medium, connecting the CNS and the C-S-H gel surface by forming inter-molecule H-bond networks.

The H-bond network established between the CNS and the C-S-H are classified as the structural hydrogen-bonding in the nanocomposite, which differ significantly from those among the water molecules[64]. The broader RDF pattern of Ow-Ho with peak position larger than 2.45 Å confirms that the hydroxyl groups of CNS are primarily gathered around the inter calcium layer at the ITZ region due to the inter- and intra-molecule H-bonds within the chain and are ultra-confined by the surrounding bulk water.

The H-bond network at ITZ can further mitigate the water dynamics at the interlayer nano-channel. The dynamics of the Hw atoms in the nanocomposite are characterized by their mean square displacement (MSD). The overall MSD evolutions of different atom chunks as a function of time are shown in Fig. S4. In comparison to the pure C-S-H model, the dynamics of neighboring water molecules are highly restrained for the nanocomposite (Fig. 7l). The translational diffusion coefficients D approximated by linear regression of the MSD curve are summarized in Table S2 for different Ca/Si ratios. The diffusion coefficient of water at the pore surface in the hydrated cement paste is approximate 1/61 of the water bulk and the

corresponding diffusion coefficient in the CNS reinforced C-S-H is much less than that in the plain C-S-H with D values fluctuating around $2.2\times10^{-11}m^2/s$ for most cases. Because the distorted chain acts as a reservoir and retains the water molecules, the hydroxyl/hydroxymethyl and methine functional groups of CNS that are deeply embedded into the bulk water act like a root network cross-linked to the neighboring silicate calcium layer, which blocks the water channels, thus inhibiting the water movement. It is worth mentioning that the rapid streaming of water in the nano-channel in the C-S-H can produce a strong repulsive force and fluid pressure that disturb the chemical bonds in the C-S-H and weaken the connections between the neighboring calcium silicate layers[65]. Therefore, one significant benefit of using CNS is to stabilize the interlayer water, reduce the flowability of the composite material and strengthen the interfacial connection.

3.3 Atomistic simulations of C-S-H/CNS mechanical behavior

The stress-strain curves of the nanocomposites when they are subjected to uniaxial tension/compression provide insights into the constitutive relationships of the materials at the atomic scale. Taking Ca/Si=1.7 as an example, the plain C-S-H shows distinct anisotropic mechanical behaviors as depicted in Fig. 8a. As shown, when subjected to tension, C-S-H exhibits a ductile behavior in both the *x*- and *y*- directions and a brittle behavior in the *z*-direction. The tensile strength of the C-S-H structure in the *x*- direction is due to the interaction between the silicate tetrahedra and the calcium clusters. The C-S-H structure in the *y*- direction provides the highest strength as the long silicate chain growing along the *y*-direction contributes significantly to the tensile resistance. However, in the *z*- direction, the presence of water in the C-S-H nano-pore weakens the Ca-O-Si bonding between neighboring calcium silicate layers by isolating the calcium ions from the surrounding oxygen atoms. The segregation generally occurs at this interlayer region during tensile loading, thus showing the lowest tensile strength. For compressive behavior, there are no significant differences among the three directions.

Fig. 8b-d compares the stress-strain curves between the pure C-S-H and the bilayer C-S-H/CNS nanocomposite along the *x*-, *y*- and *z*- directions, respectively. It can be clearly seen that CNS has a significant impact on the mechanical response of C-S-H when subjected to uniaxial tension or compression. A discernible higher stiffness is observed in the elastic stage in the bilayer C-S-H/CNS nanocomposites for all the three directions. This is due to the contribution of the relative high Young's modulus of the CNS crystal (computed as 128GPa in the current work). In addition, the strength and the ductility are increased in both tension and compression.

In the *x*- direction (Fig. 8b), the reinforcing effect of CNS is significant where the peak stress is increased by approximate 50%. This is because the CNS chain is parallel to the tensile loading direction, thus providing a crack bridging effect in C-S-H, which in return helps transfer the stress between the defective silicates. In addition, the strong C-C covalent bond and the C-O-C glucose linkage within the CNS backbone resist mechanical deformation in the *x*-direction. For compression, the compressive stress-strain curve of the C-S-H/CNS nanocomposite is similar to that of the plain C-S-H with a moderate increase in the compressive strength up to around 23% for Ca/Si=1.7.

In the *y*- direction (Fig. 8c), the tensile strength of the C-S-H is increased by approximately 16%, primarily due to the contribution of the inter-molecular H bond connections (O2-HO2…O6) between the adjacent CNS chains. The reinforcing effect of the CNS in the y-direction only exists in the pre-peak region, because the inter-molecular H bond connections between the adjacent chains can be easily ruptured at small deformations. As such, the C-S-H nanocomposite exhibits similar post-peak performance to that of the plain C-S-H gel but with higher stiffness and tensile strength in the pre-peak region. The shape of the compressive stress-strain curve of the C-S-H/CNS nanocomposite is also similar to that of the C-S-H and shows increase in the compressive strength by up to 25%.

In the *z*- direction (Fig. 8d), the tensile strength of the C-S-H/CNS nanocomposite under

tension is slightly higher than the tensile strength of the plain C-S-H (see Table S3). The insertion of CNS into C-S-H also increases the tensile deformation of the C-S-H/CNS nanocomposite in the post-failure region between 0.1 and 1.0 Å/Å. This means that the inclusion of CNS improves of the ductility of the C-S-H along the interlayer direction due to the plasticity feature of CNS. As previously discussed, the presence of CNS provides more Ca-O coordination and donates H-bond to the neighboring calcium silicate layer, thus improving the interfacial bond between the silicate layers. In addition, as the water in the C-S-H layers migrates to CNS, calcium ions that previously shielded by the water molecules are now free to form more amorphous Ca-O connection networks, thereby further strengthening the interface between the silicate layers. This results in an increase in the tensile strength of about 20% (see Fig. 8d and Table S3). The improvement in the compressive behavior of the C-S-H/CNS nanocomposite is much more evident in the *z*- direction. This is because the CNS monolayer lying in the *x*-*y* plane restrains the lateral dilation of the structure. The compressive strength of the C-S-H/CNS nanocomposite is increased by 36% (Fig. 8d and Table S3). The compressive stress-strain response of the C-S-H/CNS nanocomposite is characterized by an apparent strain hardening phenomenon in the post-peak response due to the passive confinement from CNS.

Fig. 8e illustrates the typical evolution of the structural morphology of the C-S-H and C-S-H/CNS nanocomposites under tension in the *x*- direction with Ca/Si=1.7. The tensile stress-induced damage processes are compared at strain levels of 0.16, 0.48, 0.80, 1.2 ÅÅ^{-1}.

As shown in Fig. 8e, the pure C-S-H and the bilayer C-S-H/CNS nanocomposites exhibit different damage processes. During tensile loading in the *x*- direction, as the strain increases, the layered structure of the pure C-S-H is slightly disturbed at the beginning, indicated by rearrangements of the silicate tetrahedral structure. When the strain reaches 0.4 ÅÅ^{-1}, micro cracks start to nucleate between the silicate layers and then coalesces into a vertical macro crack. This leads the failure of the C-S-H system. For the C-S-H/CNS nanocomposite, the

CNS monolayer remains flat in the interlayer region at all the strain levels. At the beginning of the tensile loading, the carbon-carbon and carbon-oxygen covalent bonds in the CNS chains are elongated together with the C-S-H matrix. As previously mentioned, the interfacial connection between the CNS and the C-S-H substrate is primarily controlled by the Ca-O ionic bonds and H-bonds, which are weaker than the C-O-C glucose bonds as well as C-C and C-O covalent bonds within the CNS. As a result, the CNS chain is gradually pulled out from the interlayer region during the continuous loading process. Even though a large number of functional groups grafted on the CNS surface can provide sufficient oxygen sites and donate H-bonds necessary to adhere to the calcium silicate sheet, the ITZ between the CNS and the C-S-H surface still remains as one of the weakest links in the nanocomposite system. Therefore, as the strain is continuously increased, the ionic bonds are steadily broken and the tensile stresses undertaken by the non-bonded electrostatic interaction are gradually transferred to the CNS chain, resulting in a "friction-like effect" between the CNS chains and the surrounding C-S-H substrate. Consequently, the mechanical behavior in terms of strength and post-peak ductility are dramatically improved. When the strain reaches 1.2 $ÅÅ^{-1}$, the calcium silicate sheet in the bilayer C-S-H/CNS nanocomposite remains intact and only a nanopore sized vacancy appears after the pullout of the CNS chains. On the other hand, a complete fracture is observed in the pure C-S-H with a huge crack opening at the center. The entire failure processes and the corresponding morphologies and descriptions in the *y*- and *z*-directions are illustrated in Fig. S5 and S6, respectively, in the supporting information.

The deformation simulation results at nano-scale provide molecular insights into the interfacial property between the C-S-H and the CNS, which is the origin of enhanced macro mechanical properties observed in our experiments.

During tension, the typical bond length evolutions (BLE) and the bond angle distributions (BAD) for the bilayer C-S-H/CNS nanocomposite with Ca/Si=1.7 is demonstrated by the probability density distribution. The relation between mean bond

length/angle values versus tensile strain are plotted in Fig. 9. Here, we focus on analyzing the C-C and C-O bond in the CNS backbone chain to probe its contribution to the strain evolution in the *x*- direction. For the *y*- and the *z*- directions, the BLE and BAD are shown in Fig. S7 and S8 in the supporting information. Fig. 9a shows the BLE of the C-C bond in the glucopyranose ring from a strain level of 0.04 ÅÅ^{-1} to 0.4 ÅÅ^{-1} in the *x*- direction. The distributions of the BLE are gradually shifted towards the right with an increase in the strain level, indicating that the lengths of the C-C bonds have been increased during the tensile deformation. The mean C-C bond length is slightly increased from 1.527 Å to around 1.555 Å due to the strong covalent bond between the carbon atoms. However, the BLE of the C-O bond is much more significant. As clearly seen from Fig. 9b, the C-O bond length increases steadily from 1.46 Å to 1.54 Å, suggesting that the glucose linkage (C1-O1-C4) and the epoxy linkage (C1-O5-C5) are much weaker than the carbon-carbon bond in the CNS. When viewed in conjunction with the corresponding BAD shifts, the reorientation of the CNS structure simultaneously occurs to adapt to the increasing strain, rather than merely bond-stretching. It can be seen from Fig. 9c that the BAD of the C-C-C shows a much broader distribution (from 80 to 140 deg) during the continuous loading with minor variations of the mean bond angles from 104.5 to 106.5 deg. This implies that the glucopyranose ring undergoes in-plane stretching together with a strong distortion of the hexagonal saccharide unit. From the C-O-C linkage shown in Fig. 9d, we can see that the BAD moves significantly towards the right with a significant change in the mean bond angle from 115 to 124 deg. This is responsible for the elongation of the CNS chains. The distortion of the CNS chains and stretching of glycosidic bonds occurring during the early load bearing process contribute to the increase in the nanocomposite stiffness due to the high modulus of CNS.

From Fig. 10, both the mean bond length and the mean bond angle increase proportionally with the strain increment until the structure is stretched to the peak strain level of around 0.2 Å. Subsequently, a plateau with slight oscillation is observed as the strain

gradually increases. No significant change in bond characteristics occur after the peak strain, confirming that in the *x*- direction, the CNS maintains its deformed shape and is gradually pulled out from the C-S-H substrate during the tensile loading. This is due to a higher tensile strength of the CNS in the *x*- direction in comparison to that of the pure C-S-H.

Fig.11 shows the stress-strain responses of the C-S-H and C-S-H/CNS nanocomposite in the *x*- direction at different Ca/Si ratios. The stress-strain responses of all samples in the *x*-, *y*-, *z*- directions are summarized in Fig. S9 and their maximum tensile and compressive stresses are tabulated in Table S3 in the supporting information. From Fig. 11a, the mechanical properties (i.e., stiffness and tensile and compressive strength) of C-S-H are gradually decreasing with increasing the Ca/Si ratio. A similar trend is also observed in the C-S-H/CNS nanocomposite as shown in Fig. 11b. This is due to the fact that the degree of defectiveness of C-S-H increases with an increase in the Ca/Si ratio, thus resulting in lower mechanical properties.

Fig. 11c,d depicts the effectiveness of CNS in strengthening defective C-S-H structures in the *x*- direction where the tensile and compressive stresses are applied along the CNS chain direction. As shown in Fig. 11c, the CNS heals defective C-S-H structures by improving their tensile strength. For example, the tensile strength of the plain C-S-H is increased due to the inclusion of CNS by as much as 36.32% at Ca/Si = 1.1 (i.e., lowly-defective C-S-H) and 74.98% at Ca/Si = 2.1(i.e., highly-defective C-S-H) (see Table S3). Under compression (see Fig.11d), the CNS seems to heal the defective C-S-H structures with Ca/Si ratios higher than 1.3 where the compressive strength of the C-S-H is increased by as much as 30.37% at Ca/Si = 2.1 (see Table S3).

The healing effect of CNS in the *y*- direction is shown in Fig. S9. A moderate increase in the tensile strength (between 10%~17%) is obtained for the C-S-H/CNS with Ca/Si ratios higher than 1.5. The increase in the compressive strength is between 20%-30% over the Ca/Si ratio range. In the *z*- direction, the increase in the tensile strength reaches up to 35% when the

Ca/Si ratio is 2.1, which is much higher than that in the *y*- direction. This is attributed to the ionic bonds established between the CNS functional groups and the calcium silicate sheets. Similar to the trend in tension, the C-S-H/CNS nanocomposite shows significant increase in the compressive strength, between 24.13% and 41.42% over the Ca/Si ratio range. The above findings indicate that overall, the CNS is more effective in healing highly-defective C-S-H, the main hydration phase of OPC than lowly-defective C-S-H. Table S3 summarizes the percentage of strength increase under tension and compression for all samples.

4. Conclusion

We have demonstrated the feasibility of using carrot-based cellulose nanosheets, sourced from inexpensive biomass, as a low-cost and environmentally friendly material for reinforcing highly deficient C-S-H, the main hydration product of cement. We performed MD simulations in conjunction with experimental characterization to gain fundamental understanding of the reinforcement effect of the CNS inserted into C-S-H with different Ca/Si ratios and uncover the interaction mechanisms at the atomic level between C-S-H and the CNS. Based on the combined MD simulations and experimental characterization, the following conclusions can be drawn:

(1). The CNSs show remarkable affinity to C-S-H due to the interfacial Ca-O coordination and H-bond interaction. The functional groups on the surface of the CNS were found to act like a root network confined by the surrounding bulk water molecules at the ITZ, thereby cross-linking the neighboring silicate calcium layers. This significantly improves the interfacial properties of the C-S-H/CNS hybrid structure. We also discovered that the water molecules between the C-S-H structures tend to migrate towards the intercalated CNSs. The water migration towards CNS transforms the layered C-S-H structure into a more amorphous state with increased interfacial Ca-O coordination number, thereby producing better structural stability and stronger interfacial properties. The retained water molecules in the CNS can further mitigate the water dynamics at the silicate nanochannel. As such, the water streaming

effect can be reduced and the cohesive force of the C-S-H gel can be improved.

(2). The incorporation of the CNSs can considerably improve the anisotropic constitutive behavior of C-S-H in terms of strength, stiffness and post-peak ductility at nano-scale. When the hybrid C-S-H/CNS structure is tensioned along the CNS chain direction, the tensile strength of the nanocomposite is increased by up to 75%, depending on the Ca/Si ratio. The reinforcing effect becomes more pronounced for disordered C-S-H structures. This is significant, because the poor performance of current cement-based materials is due to defective C-S-H gels resulting from high Ca/Si ratios. Thus, incorporating CNSs into cementitious materials would eliminate the need for costly and exhausting manufacturing processes to change the chemistry of the cement ingredients to achieve lower Ca/Si ratios for enhanced performance.

(3). The addition of the CNSs increases the compressive strength of C-S-H when the nanocomposite is loaded along the *z*- direction and perpendicular to the CNS surface. An increase up to 40% is achieved at the highest Ca/Si ratio. The addition of CNSs also enhances the compressive ductility of the C-S-H nanocomposite due to the strain-hardening effect resulting from the continuous confinement effect.

(4). Our experimental results clearly demonstrate that atomic-scale reinforcing mechanisms significantly improve the micro and macroscale properties of the cementitious composites containing CNSs sourced from inexpensive carrot waste streams. Compared to the plain cementitious composite, the nanocomposite with CNSs exhibited denser and better packed microstructure. The micromechanical properties of the nanocomposites are also improved when the CNSs are present. This improvement is more pronounced for the flexural strength due to the crack bridging effect.

The C-S-H reinforcement approach introduced here will aid efforts to design new generations of concrete materials with lower carbon footprint, by lowering the associated CO_2 emissions during cement production for the construction industry. When compared to current

cement reinforcing materials such as CNTs, graphene, GO and h-BN, the proposed CNS reinforcing material is inexpensive, renewable, carbon neutral, and has low environmental, health and safety risks. Furthermore, the CNSs are readily dispersible in water without the use of surface modification or surfactant and more importantly are highly compatible with C-S-H, the main hydration phase of cement. These features identify CNSs as a promising material for the production of sustainable and high-performance concretes. By increasing the performance of concrete, structural concrete elements with smaller sizes can be designed, thus reducing the volume of concrete, which in return reduces the energy and carbon intensity of the cement in the construction industry.

Data availability statement

The raw/processed data required to reproduce these findings cannot be shared at this time as the data also forms part of an ongoing study.

Acknowledgement

This research work is financially supported by the European Commission Horizon 2020 Marie Sklodowska-Curie Research Grant (B-SMART 799658). The authors would like to thank Cellucomp Ltd, Burntisland, UK for designing and manufacturing the CNSs. The authors are also grateful for the support from the China International Collaboration Fund (G20190017133).

Reference

[1] Monteiro PJM, Miller SA, Horvath A. Towards sustainable concrete. Nat Mater 2017;16:698–9.

[2] Norhasri MSM, Hamidah MS, Fadzil AM. Applications of using nano material in concrete: A review. Constr Build Mater 2017;133:91–7.

[3] Senff L, Tobaldi DM, Lucas SS, Hotza D, Ferreira VM, Labrincha JA. Formulation of mortars with nano-SiO 2 and nano-TiO 2 for degradation of pollutants in buildings. Compos Part B Eng 2013;44:40–7.

[4] Zhu Z, Xu W, Chen H, Tan Z. Evolution of microstructures of cement paste via continuous-based hydration model of non-spherical cement particles. Compos Part B Eng 2020;185:107795.

[5] Xue G, Yilmaz E, Song W, Cao S. Mechanical, flexural and microstructural properties of cement-tailings matrix composites: effects of fiber type and dosage. Compos Part B Eng 2019;172:131–42.

[6] Shahsavari R. Intercalated Hexagonal Boron Nitride/Silicates as Bilayer Multifunctional Ceramics. ACS Appl Mater Interfaces 2018;10:2203–9.

[7] Yang H, Cui H, Tang W, Li Z, Han N, Xing F. A critical review on research progress of graphene/cement based composites. Compos Part A Appl Sci Manuf 2017;102:273–96.

[8] Zhou C, Li F, Hu J, Ren M, Wei J, Yu Q. Enhanced mechanical properties of cement paste by hybrid graphene oxide/carbon nanotubes. Constr Build Mater 2017;134:336–45.

[9] Lv SH, Deng LJ, Yang WQ, Zhou QF, Cui YY. Fabrication of polycarboxylate/graphene oxide nanosheet composites by copolymerization for reinforcing and toughening cement composites. Cem Concr Compos 2016;66:1–9.

[10] Li G, Zhang LW. Microstructure and phase transformation of graphene-cement composites under high temperature. Compos Part B Eng 2019;166:86–94.

[11] Qureshi TS, Panesar DK, Sidhureddy B, Chen A, Wood PC. Nano-cement composite with graphene oxide produced from epigenetic graphite deposit. Compos Part B Eng 2019;159:248–58.

[12] Gao Y, Jing HW, Chen SJ, Du MR, Chen WQ, Duan WH. Influence of ultrasonication on the dispersion and enhancing effect of graphene oxide–carbon nanotube hybrid nanoreinforcement in cementitious composite. Compos Part B Eng 2019;164:45–53.

[13] Kırgız MS. Green cement composite concept reinforced by graphite nano-engineered particle suspension for infrastructure renewal material. Compos Part B Eng 2018;154:423–9.

[14] Zhou Y, Hou D, Geng G, Feng P, Yu J, Jiang J. Insights into the interfacial strengthening mechanisms of calcium-silicate-hydrate/polymer nanocomposites. Phys Chem Chem Phys 2018;20:8247–66.

[15] Zhou Y, Hou D, Manzano H, Orozco CA, Geng G, Monteiro PJM, et al. Interfacial Connection Mechanisms in Calcium-Silicate-Hydrates/Polymer Nanocomposites: A Molecular Dynamics Study. ACS Appl Mater Interfaces 2017;9:41014–25.

[16] Shalchy F and NR. Nanostructural Characteristics and Interfacial Properties of Polymer Fibers in Cement Matrix. ACS Appl Mater Interfaces 2015;7:17278–86.

[17] Hou D, Yu J, Wang P. Molecular dynamics modeling of the structure, dynamics,

energetics and mechanical properties of cement-polymer nanocomposite. Compos Part B Eng 2019;162:433–44.
[18] Zhang W, Zou X, Wei F, Wang H, Zhang G, Huang Y, et al. Grafting SiO2 nanoparticles on polyvinyl alcohol fibers to enhance the interfacial bonding strength with cement. Compos Part B Eng 2019;162:500–7.
[19] Yao X, Shamsaei E, Chen S, Zhang QH, de Souza FB, Sagoe-Crentsil K, et al. Graphene oxide-coated Poly (vinyl alcohol) fibers for enhanced fiber-reinforced cementitious composites. Compos Part B Eng 2019;174:107010.
[20] Zhou Y, Orozco CA, Duque-Redondo E, Manzano H, Geng G, Feng P, et al. Modification of poly(ethylene glycol) on the microstructure and mechanical properties of calcium silicate hydrates. Cem Concr Res 2019;115:20–30.
[21] Kumar A, Walder BJ, Kunhi Mohamed A, Hofstetter A, Srinivasan B, Rossini AJ, et al. The Atomic-Level Structure of Cementitious Calcium Silicate Hydrate – Supporting Information Table of Contents. J Phys Chem C 2017;121:17188–96.
[22] Xu L, Deng F, Chi Y. Nano-mechanical behavior of the interfacial transition zone between steel-polypropylene fiber and cement paste. Constr Build Mater 2017;145:619–38.
[23] Allen AJ, Thomas JJ, Jennings HM. Composition and density of nanoscale calcium-silicate-hydrate in cement. Nat Mater 2007;6:311–6.
[24] Chen B, Qiao G, Hou D, Wang M, Li Z. Cement-based material modified by in-situ polymerization: From experiments to molecular dynamics investigation. Compos Part B Eng 2020:108036.
[25] Hou D, Xu J, Zhang Y, Sun G. Insights into the molecular structure and reinforcement mechanism of the hydrogel-cement nanocomposite: An experimental and molecular dynamics study. Compos Part B Eng 2019;177:107421.
[26] Eftekhari M, Mohammadi S, Khanmohammadi M. A hierarchical nano to macro multiscale analysis of monotonic behavior of concrete columns made of CNT-reinforced cement composite. Constr Build Mater 2018;175:134–43.
[27] Ioannidou K, Krakowiak KJ, Bauchy M, Hoover CG, Masoero E, Yip S, et al. Mesoscale texture of cement hydrates. Proc Natl Acad Sci 2016;113:2029–34.
[28] Jennings HM, Bullard JW. From electrons to infrastructure: Engineering concrete from the bottom up. Cem Concr Res 2011;41:727–35.
[29] Ye J, Chu C, Cai H, Hou X, Shi B, Tian S, et al. A multi-scale model for studying failure mechanisms of composite wind turbine blades. Compos Struct 2019;212:220–9.
[30] Ye J, Chu C, Cai H, Wang Y, Qiao X, Zhai Z, et al. A multi-scale modeling scheme for damage analysis of composite structures based on the High-Fidelity Generalized Method of Cells. Compos Struct 2018;206:42–53.
[31] Tatar J, Taylor CR, Hamilton HR. A multiscale micromechanical model of adhesive interphase between cement paste and epoxy supported by nanomechanical evidence. Compos Part B Eng 2019;172:679–89.
[32] Birenboim M, Nadiv R, Alatawna A, Buzaglo M, Schahar G, Lee J, et al. Reinforcement and workability aspects of graphene-oxide-reinforced cement nanocomposites. Compos Part B Eng 2019;161:68–76.
[33] Kunhi Mohamed A, Parker SC, Bowen P, Galmarini S. An atomistic building block description of C-S-H - Towards a realistic C-S-H model. Cem Concr Res 2018;107:221–35.

[34] Qomi MJA, Krakowiak KJ, Bauchy M, Stewart KL, Shahsavari R, Jagannathan D, et al. Combinatorial molecular optimization of cement hydrates. Nat Commun 2014;5:4960.
[35] Pellenq RJ-M, Kushima A, Shahsavari R, Van Vliet KJ, Buehler MJ, Yip S, et al. A realistic molecular model of cement hydrates. Proc Natl Acad Sci 2009;106:16102–7.
[36] Almeida APC, Canejo JP, Fernandes SN, Echeverria C, Almeida PL, Godinho MH. Cellulose-Based Biomimetics and Their Applications. Adv Mater 2018;30:1–31.
[37] Shchipunov Y, Postnova I. Cellulose Mineralization as a Route for Novel Functional Materials. Adv Funct Mater 2018;28:1–28.
[38] Moon RJ, Martini A, Nairn J, Simonsen J, Youngblood J. Cellulose nanomaterials review: structure, properties and nanocomposites. Chem Soc Rev 2011;40:3941–94.
[39] Mazeau K, Heux L. Molecular dynamics simulations of bulk native crystalline and amorphous structures of cellulose. J Phys Chem B 2003;107:2394–403.
[40] Portugal I, Dias VM, Duarte RF, Evtuguin D V. Hydration of cellulosesilica hybrids assessed by sorption isotherms. J Phys Chem B 2010;114:4047–55.
[41] Alshaghel A, Parveen S, Rana S, Fangueiro R. Effect of multiscale reinforcement on the mechanical properties and microstructure of microcrystalline cellulose-carbon nanotube reinforced cementitious composites. Compos Part B Eng 2018;149:122–34.
[42] Hasan H, Huang B, Saafi M, Sun J, Chi Y, Whale E, et al. Novel engineered high performance sugar beetroot 2D nanoplatelet-cementitious composites. Constr Build Mater 2019;202:546–62.
[43] Chen P, Ogawa Y, Nishiyama Y, Ismail AE, Mazeau K. Linear, non-linear and plastic bending deformation of cellulose nanocrystals. Phys Chem Chem Phys 2016;18:19880–7.
[44] Rahman R, Foster JT, Haque A. Molecular dynamics simulation and characterization of graphene–cellulose nanocomposites. J Phys Chem A 2013;117:5344–53.
[45] Bergenstråhle M, Wohlert J, Himmel ME, Brady JW. Simulation studies of the insolubility of cellulose. Carbohydr Res 2010;345:2060–6.
[46] Hou D, Yu J, Jin Z, Hanif A. Molecular dynamics study on calcium silicate hydrate subjected to tension loading and water attack: structural evolution, dynamics degradation and reactivity mechanism. Phys Chem Chem Phys 2018;20:11130–44.
[47] Morshedifard A, Masoumi S, Qomi MJA. Nanoscale origins of creep in calcium silicate hydrates. Nat Commun 2018;9:1–10.
[48] Richardson IG. The calcium silicate hydrates. Cem Concr Res 2008;38:137–58.
[49] Fan D, Yang S. Mechanical properties of CSH globules and interfaces by molecular dynamics simulation. Constr Build Mater 2018;176:573–82.
[50] Hepworth D, Whale E. Cellulose platelet compositions, methods of preparing cellulose platelet compositions and products comprising same. US 9,834,664 B2, 2017.
[51] ASTM C109 A. Standard test method for compressive strength of hydraulic cement mortars (Using 2-in. or [50-mm] cube specimens). Am Soc Test Mater 2002.
[52] ASTM C. Standard test method for flexural strength of concrete (using simple beam with third-point loading). Am. Soc. Test. Mater., vol. 100, 2010, p. 12959–9428.
[53] Plimpton S. Fast parallel algorithms for short-range molecular dynamics. J Comput Phys 1995;117:1–19.
[54] Stukowski A. Visualization and analysis of atomistic simulation data with OVITO–the Open Visualization Tool. Model Simul Mater Sci Eng 2009;18:15012.
[55] Nishiyama Y, Sugiyama J, Chanzy H, Langan P. Crystal structure and hydrogen

bonding system in cellulose Iα from synchrotron X-ray and neutron fiber diffraction. J Am Chem Soc 2003;125:14300–6.

[56] Nishiyama Y, Langan P, Chanzy H. Crystal structure and hydrogen-bonding system in cellulose Iβ from synchrotron X-ray and neutron fiber diffraction. J Am Chem Soc 2002;124:9074–82.

[57] Bahafid S, Ghabezloo S, Duc M, Faure P, Sulem J. Effect of the hydration temperature on the microstructure of Class G cement: CSH composition and density. Cem Concr Res 2017;95:270–81.

[58] Hamid SA. The crystal structure of the 11À natural tobermorìte. Zeitschrift Fur Krist 1981;8:1–10.

[59] Cygan RT, Liang J-J, Kalinichev AG. Molecular models of hydroxide, oxyhydroxide, and clay phases and the development of a general force field. J Phys Chem B 2004;108:1255–66.

[60] Dauber- Osguthorpe P, Roberts VA, Osguthorpe DJ, Wolff J, Genest M, Hagler AT. Structure and energetics of ligand binding to proteins: Escherichia coli dihydrofolate reductase- trimethoprim, a drug- receptor system. Proteins Struct Funct Bioinforma 1988;4:31–47.

[61] Berendsen HJC, Grigera JR, Straatsma TP. The missing term in effective pair potentials. J Phys Chem 1987;91:6269–71.

[62] Hou D, Ma H, Zhu Y, Li Z. Calcium silicate hydrate from dry to saturated state: structure, dynamics and mechanical properties. Acta Mater 2014;67:81–94.

[63] Mead RN, Mountjoy G. a molecular dynamics study of the atomic structure of (CaO) x (SiO2) 1-x Glasses. J Phys Chem B 2006;110:14273–8.

[64] Manzano H, Moeini S, Marinelli F, Van Duin ACT, Ulm F-J, Pellenq RJ-M. Confined water dissociation in microporous defective silicates: mechanism, dipole distribution, and impact on substrate properties. J Am Chem Soc 2012;134:2208–15.

[65] Bonnaud PA, Ji Q, Coasne B, Pellenq R-M, Van Vliet KJ. Thermodynamics of water confined in porous calcium-silicate-hydrates. Langmuir 2012;28:11422–32.

Figures

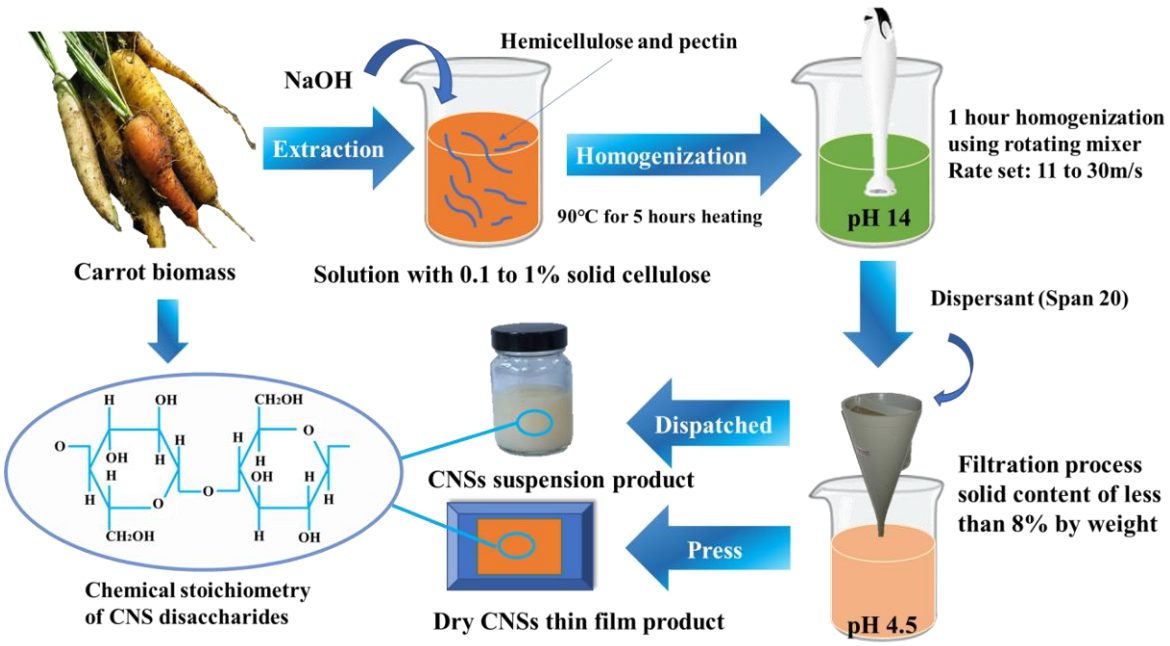

Fig.1 Schematic diagram of CNSs fabrication process

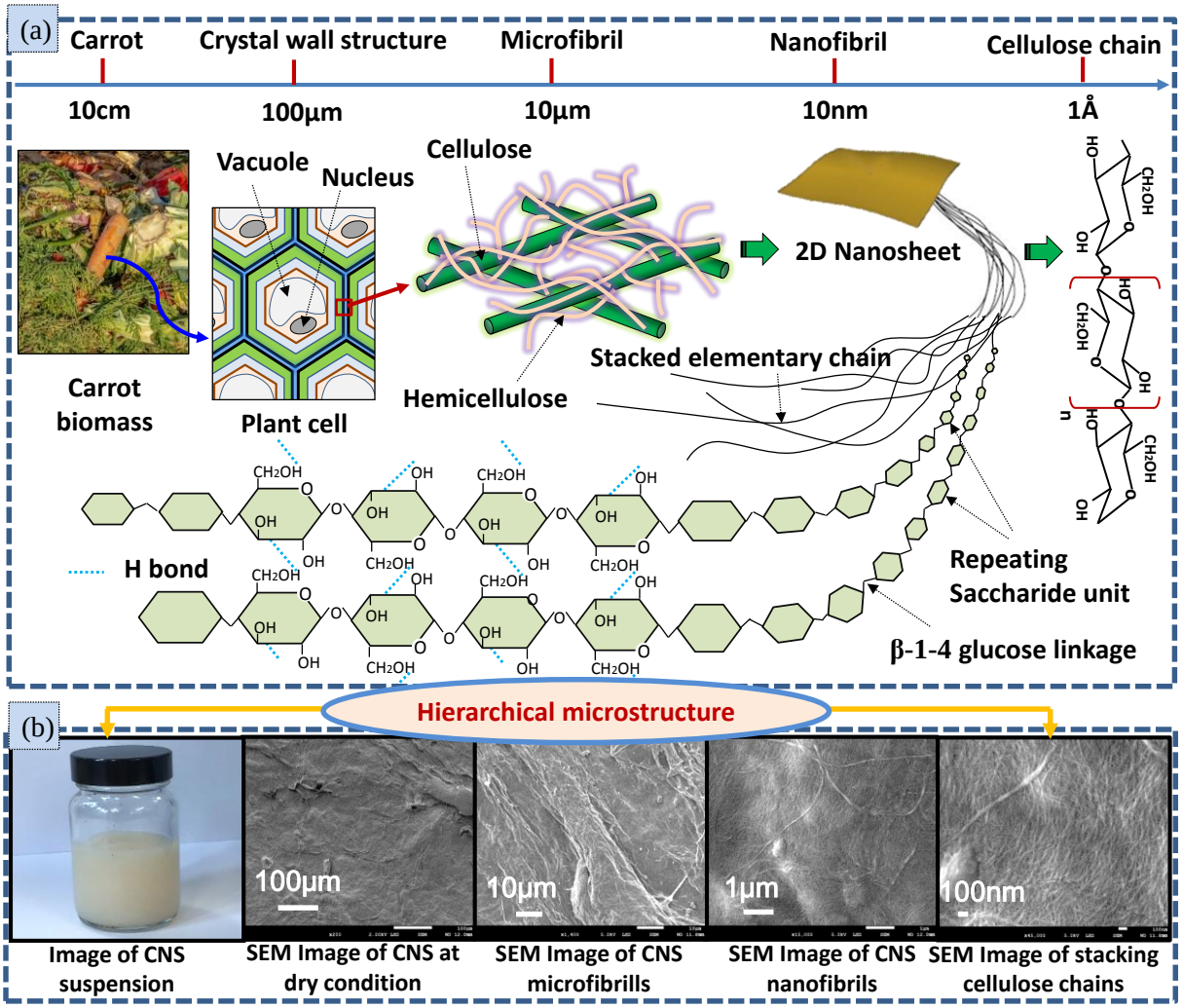

Fig. 2. The crystallographic of the 2D CNS sheets from waste stream: (a) Hierarchical microstructure of the CNS. (b) Images of the CNS from a CNS suspension to nanofibrils forming CNS at different length scales.

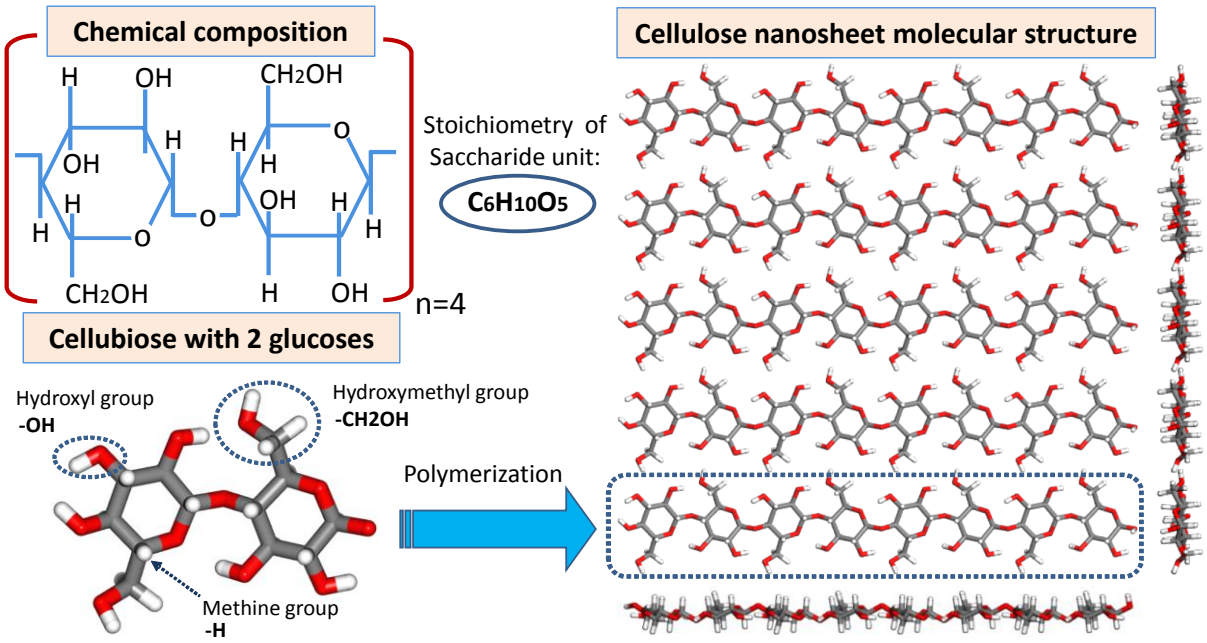

Fig. 3. Molecular structure of the CNS and the corresponding chemical stoichiometry of one saccharide unit. The black, red and white sticks in the molecular model of CNS represent carbon, oxygen and hydrogen atoms respectively.

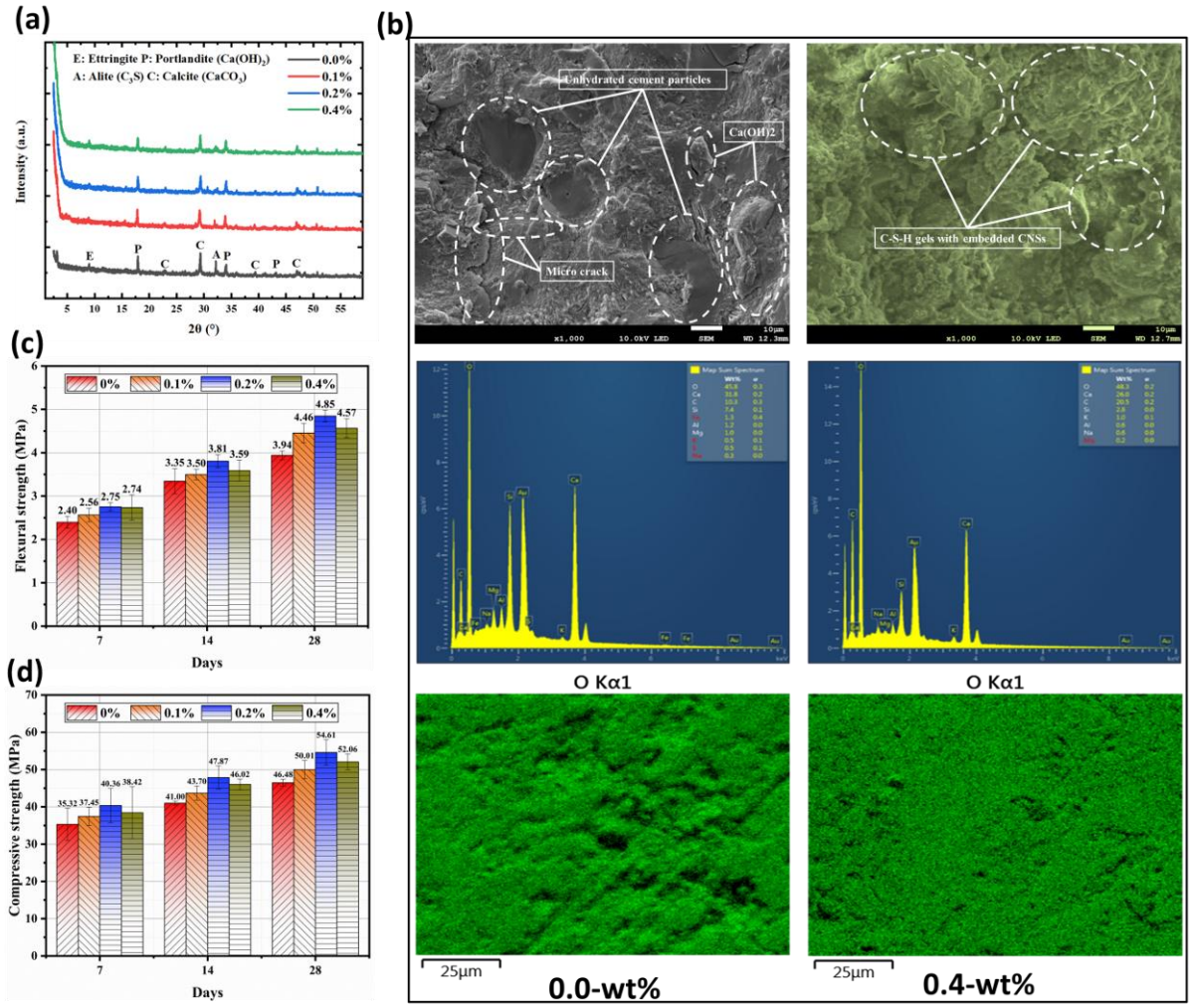

Fig. 4. Microstructure characterization and mechanical properties of CNS cementitious composites with different CNS mass fractions. (a) XRD patterns. (b) SEM-EDX images. (c) Flexural strengths. (d) Compressive strengths.

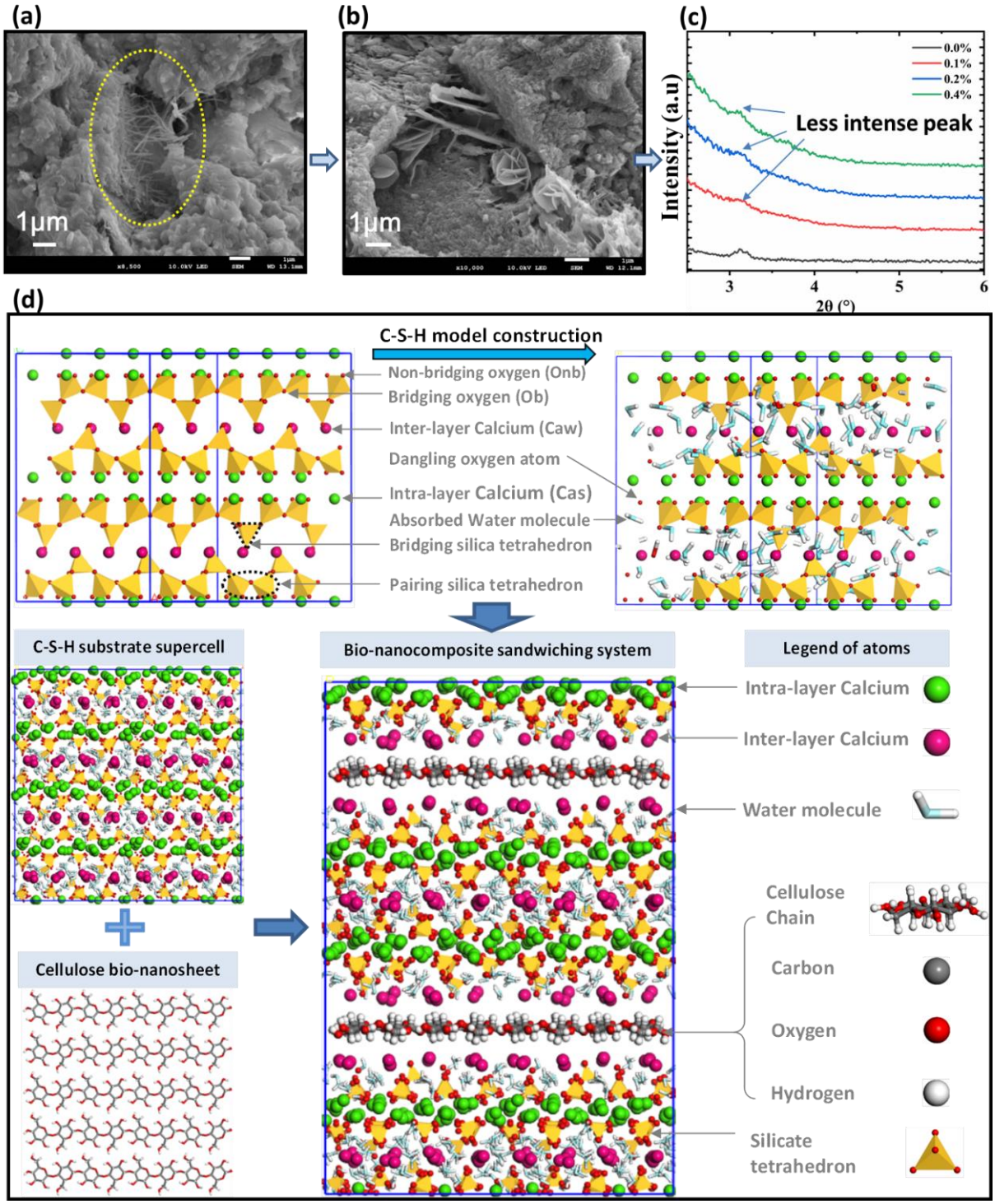

Fig. 5. Microstructural configurations of the nanocomposite. (a-b) SEM images of intercalated cellulose chain and CNS. (c) XRD patterns showing the concentration of CNS with a broader and less peak at ≈3º 2θ. (d) Constructed molecule model for nanocomposite bilayer system.

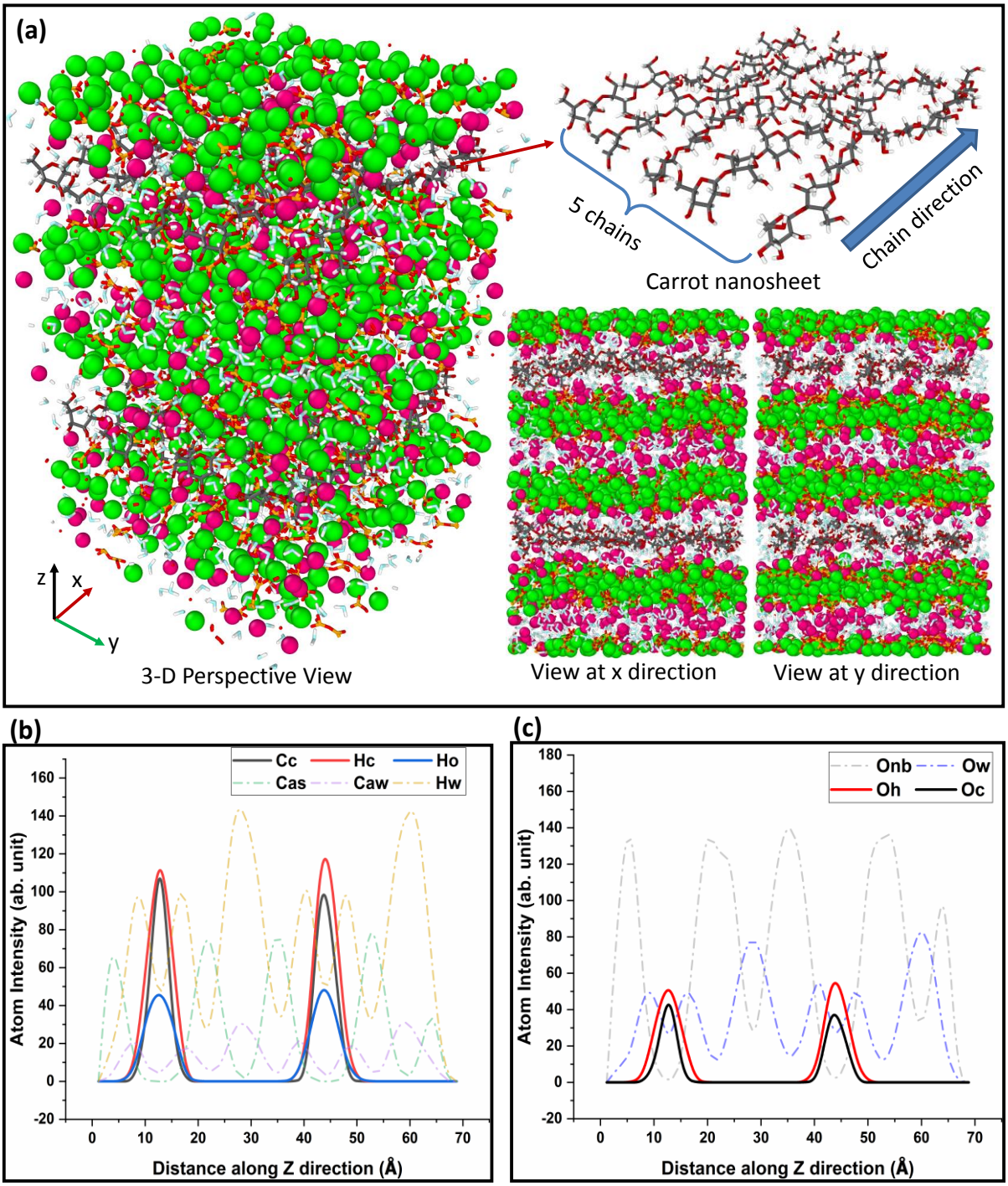

Fig. 6. Relaxed molecular structural configuration. (a) Evolved molecular model after NPT equilibrium. (b)Atom intensity distributions of different atoms at the ITZ region. (c) Atom density distributions of oxygen species from both CNS and C-S-H gel. In the atomistic configurations, the green and purple spheres represents the inter- and intra-layer calcium atoms, red balls denote the oxygen atom, black balls are the carbon atom, white balls shows the hydrogen atoms, light blue-white ball stick model represents the water molecule, yellow-red bond denotes the silicate chain(Si-O), black-red-white stick model represents the CNS chain, yellow tetrahedral shaped models are the silicate tetrahedra.

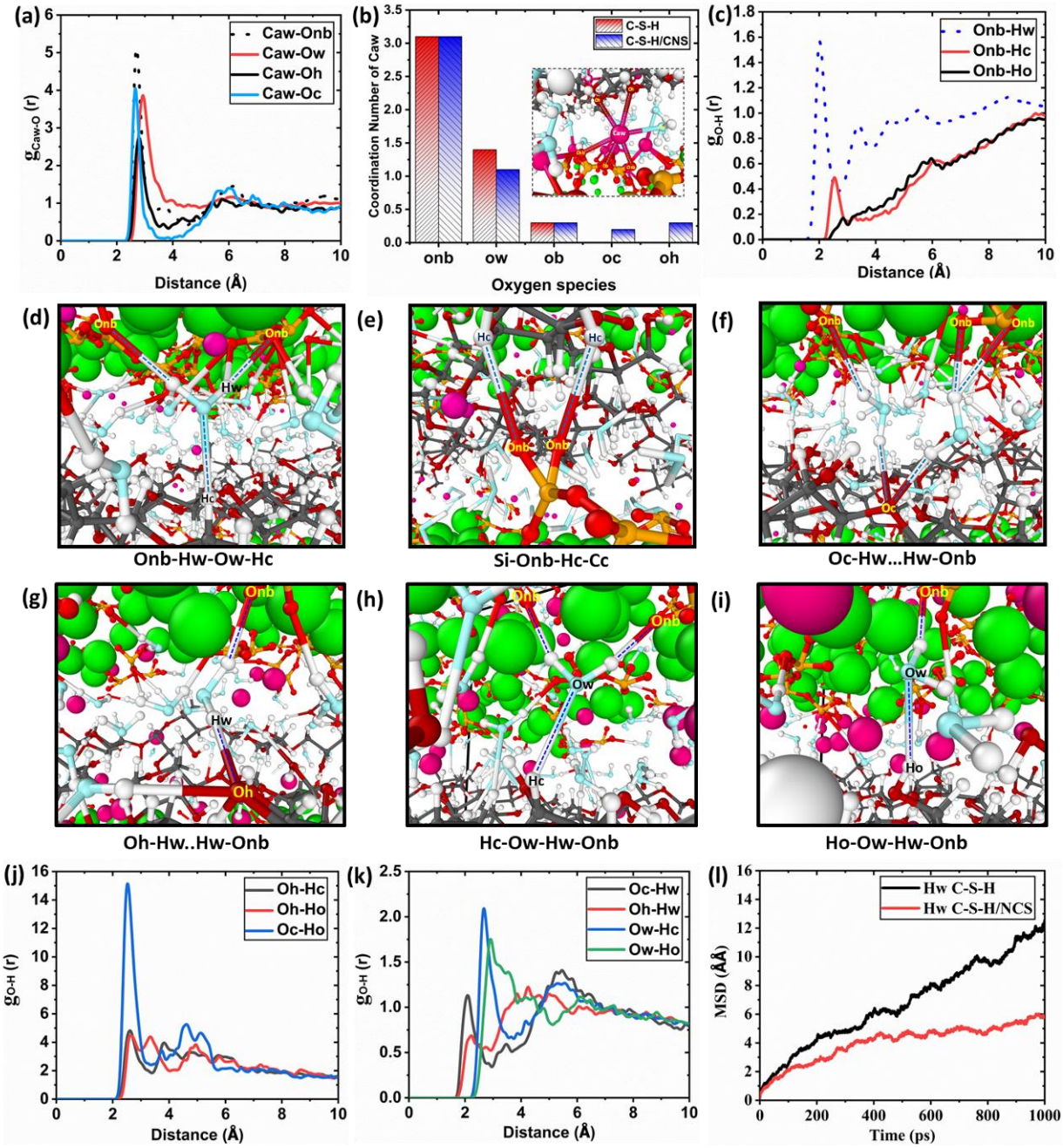

Fig. 7. Local structural characteristics of CNS at the ITZ. (a) Partial RDF between interlayer calcium from C-S-H versus different oxygen species. (b) Coordination number of different O species for pure C-S-H and nanocomposite. (c) Partial RDF between Onb versus different hydrogen Species. (d-i) Representative H-bond network in the ITZ region. (j) Partial RDF distribution between oxygen species and hydrogen species within CNS. (k) Partial RDF between oxygen and hydrogen atoms from CNS and water molecule. (l) Comparison of MSD evolution of interlayer water hydrogen atoms for the molecular systems with and without CNS. In the atomic configuration, the green, purple, yellow, red, light blue, black, dark red, white spheres represent the intra-layer calcium, inter-layer calcium, silicon, silicate oxygen, water oxygen, carbon, CNS oxygen, hydrogen atoms respectively.

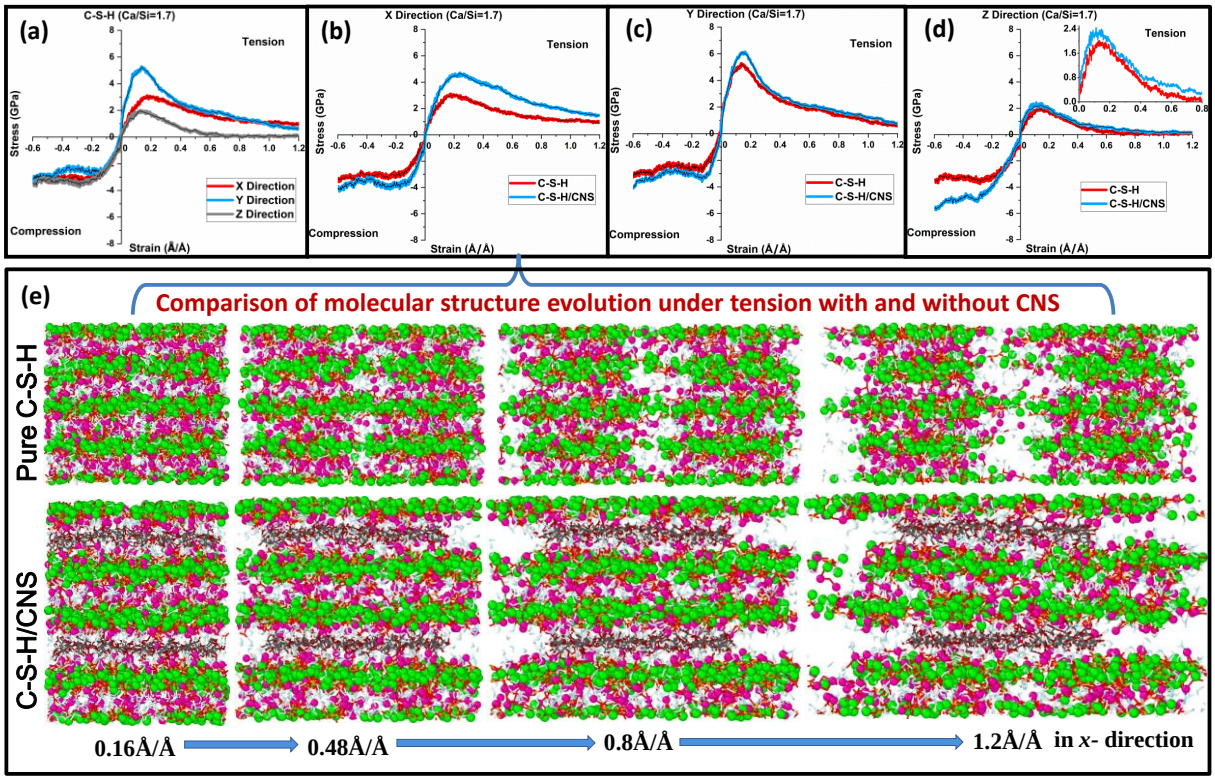

Fig. 8. Anisotropic nanomechanical properties. (a-d) Comparison of the computed stress-strain curves between the C-S-H and nanocomposite along *x*-, *y*- and *z*- direction under uniaxial deformation with Ca/Si=1.7. (e) Comparison of typical molecular structural evolutions under tension in *x*- direction. For the colored molecular configuration, the green and purple spheres represents the inter- and intra-layer calcium atoms, red balls denote the oxygen atom, light blue-white ball stick model represents the water molecule, yellow-red bond denotes the silicate chain(Si-O), black-red-white stick model represents the CNS chain.

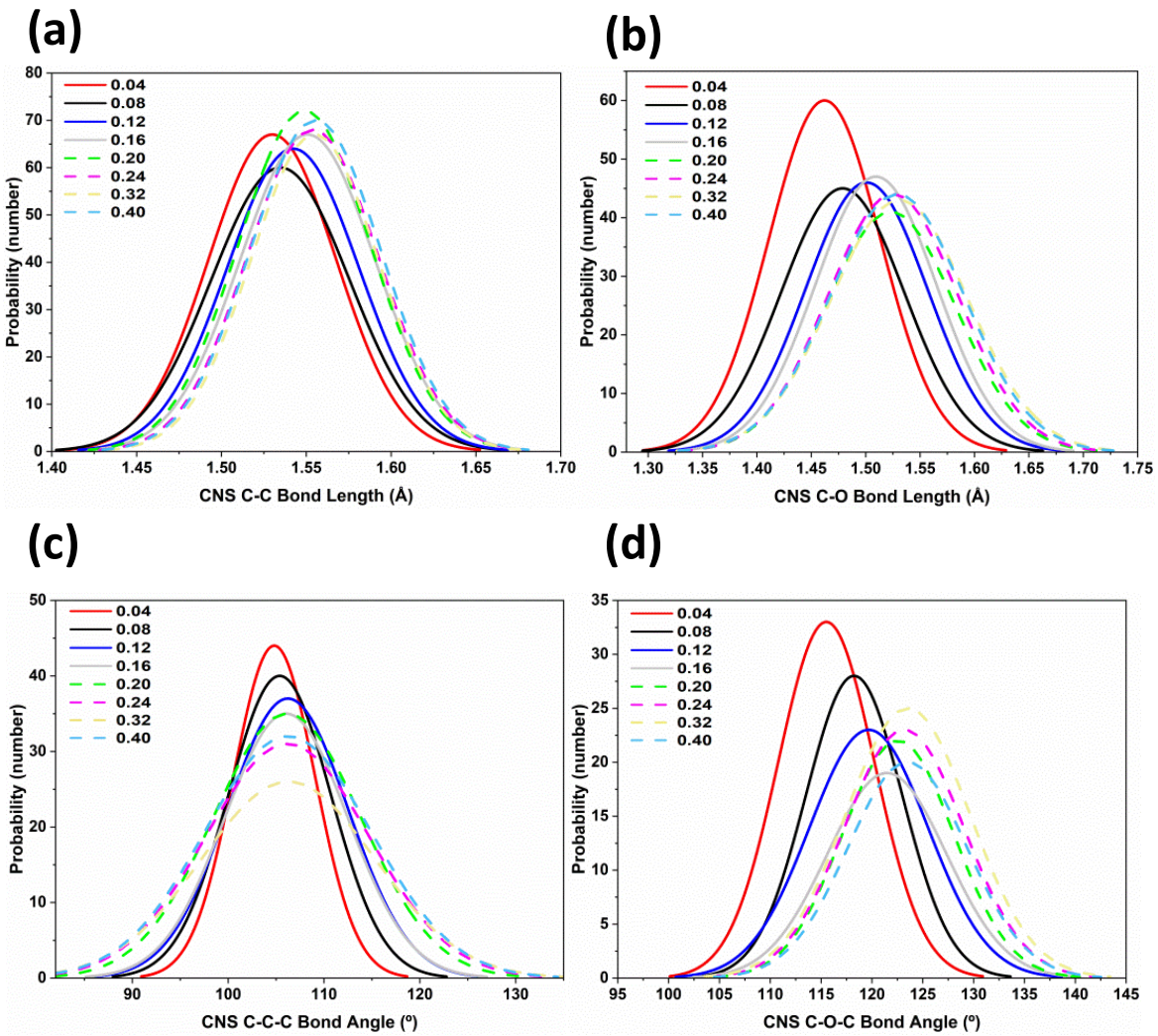

Fig. 9. BLE and BAD distributions of CNS chain during loading (a)C-C bond length distribution. (b) C-O bond length distribution. (c) C-C-C bond angle distribution. (d) C-O-C bond angle distribution.

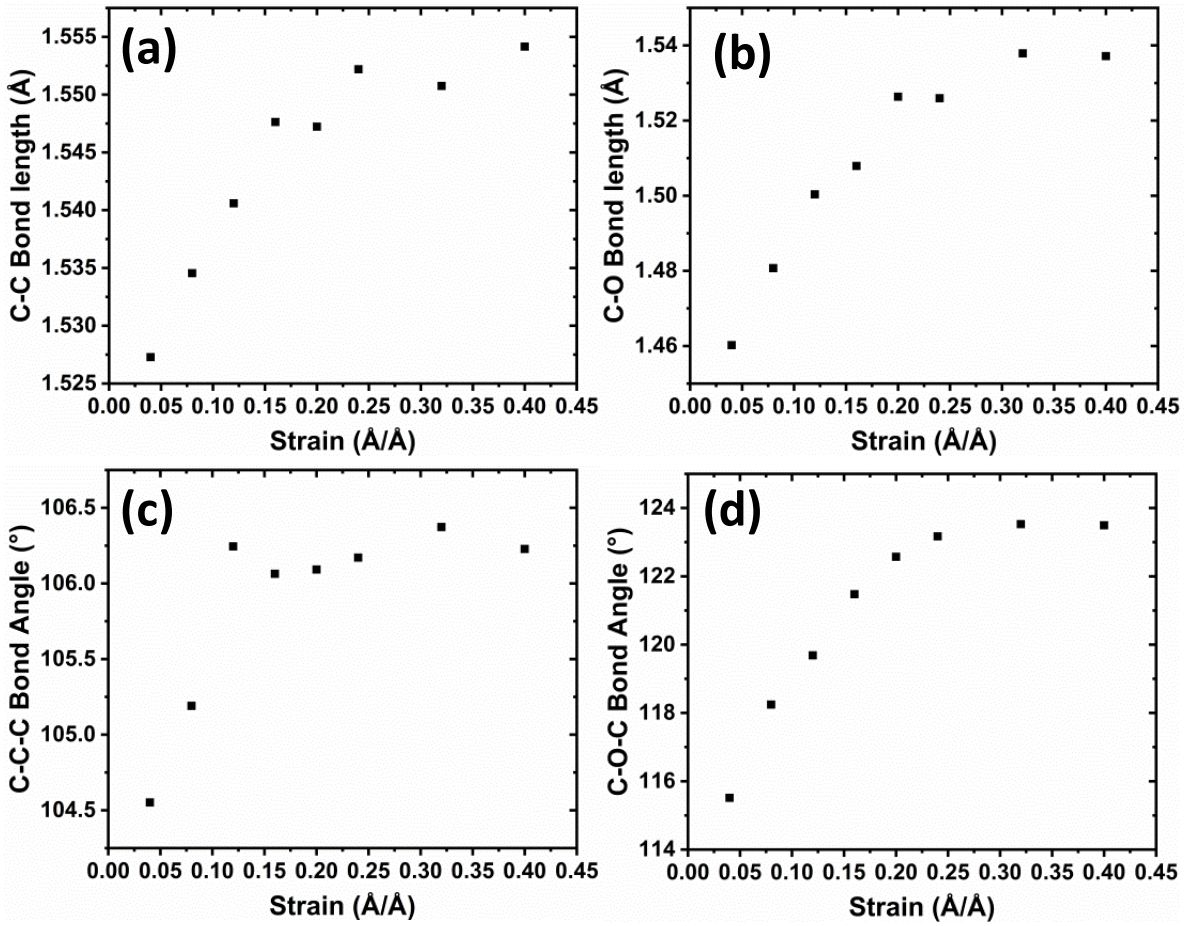

Fig. 10. Evolution of mean bond length/angle values with increasing tensile strain (a) C-C bond length evolution. (b)C-O bond length evolution. (c) C-C-C bond angle evolution. (d) C-O-C bond angle evolution.

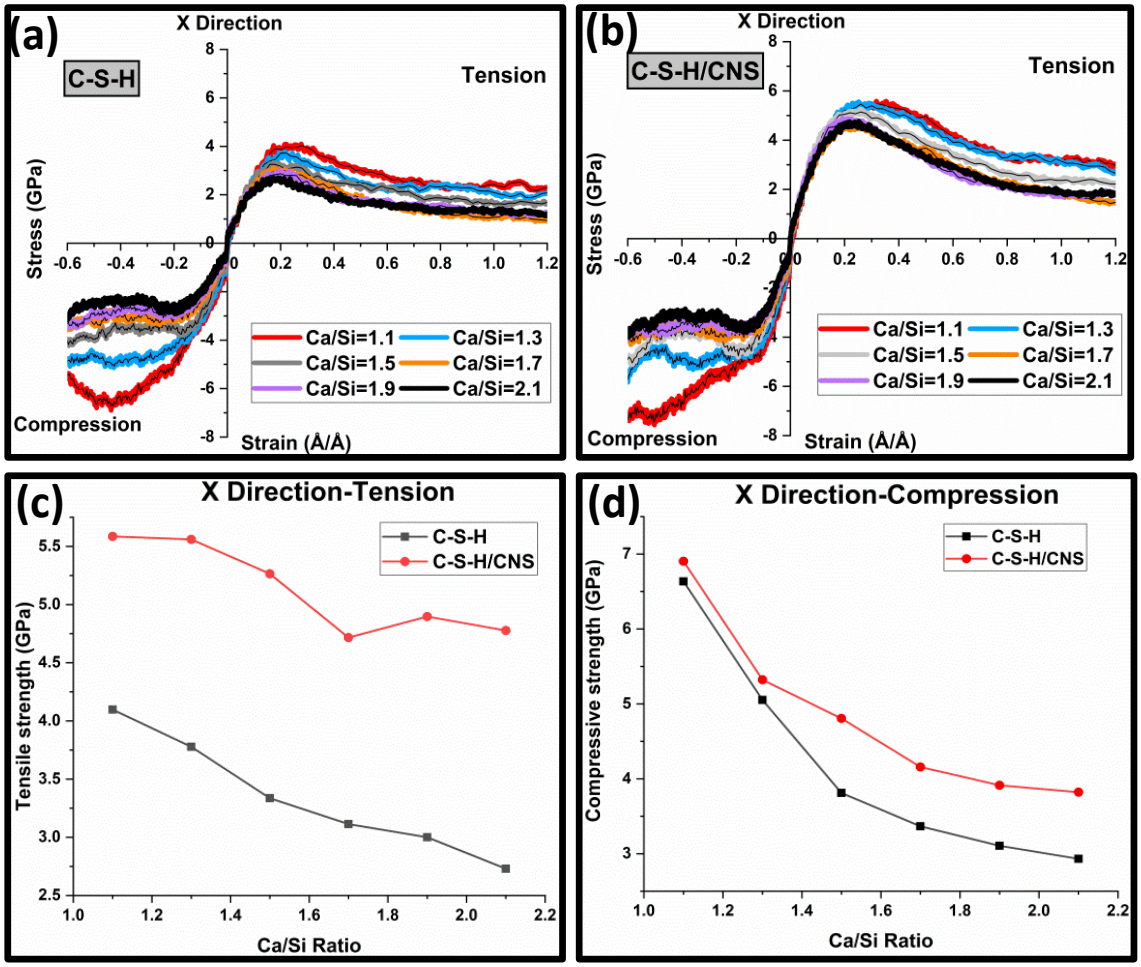

Fig. 11. Variation of nanomechanical behavior at different Ca/Si ratios. (a-b) Stress-strain responses of the C-S-H and C-S-H/CNS nanocomposite in the *x*- direction. (c-d) The effectiveness of CNS in strengthening defective C-S-H structures in the *x*- direction for tension and compression

Supporting Information

The following files are available free of charge. Supporting information (Word).

Do not remove this file (contains research data)

Click here to access/download
RDM Data Profile XML
DataProfile_4755980.xml

Declaration of interests

☒ The authors declare that they have no known competing financial interests or personal relationships that could have appeared to influence the work reported in this paper.

☐The authors declare the following financial interests/personal relationships which may be considered as potential competing interests:

Mohamed Saafi：Conceptualization, Writing - Review & Editing, Supervision, Funding acquisition. **Yin Chi**：Methodology, Software, Formal analysis, Writing - Original Draft, **Bo Huang:** Investigation, Resources, Data Curation. **Jianqiao Ye:** Validation, Writing - Review & Editing and Project administration. **Colin Lambert:** Writing - Review & Editing

Click here to access/download
Supporting File
composite part B-supporting information-31-03-2020_final_ms.docx